of mice that were treated with micelle ADR was not significantly affected by TβR-I inhibitor (data not shown). These findings in normal organs strongly suggest that low-dose TβR-I inhibitor enhances EPR effect only in tumors and that exacerbation of toxicity or side effects of nanocarrier-encapsulated drugs may be minimal with this treatment.

Discussion

In the present study, we have tested a use of TβR-I inhibitor at a low dose to induce alteration in cancer-associated neovasculature to exhibit more leakiness for macromolecules, with less pericyte-coverage and greater endothelial area (Figs. 1 and 2). Because use of TβR-I inhibitor induced the same alteration in neovasculature in the Matrigel plug assay (M.R.K., unpublished data), a model of adult neoangiogenesis (23), the effects of use of TβR-I inhibitor on tumor vasculature observed in the present study may be common in adult neoangiogenesis. Although the roles of growth factors, including TGF-β, may differ during development and in adults, these phenotypes are reminiscent of those of knockout mice deficient in certain components of TGF-β signaling, e.g., endoglin (28, 29), ALK-1 (30, 31), and ALK-5 (32), in which loss of pericyte-coverage and dilatation of the vasculature in yolk sac or embryos were observed. These phenotypes are also consistent with the findings obtained on *in vitro* culture of endothelial cell lineages (33) and mesenchymal progenitor cells (34), which showed that pericyte maturation is promoted, and endothelial proliferation is inhibited, by TGF-β signaling. Vascular phenotypes due to defects in TGF-β signaling *in vivo* are also observed in two types of hereditary hemorrhagic telangiectasia (35, 36), which are induced by deficiencies of endoglin or ALK-1, which are components of TGF-β signaling in vascular endothelium. Because of inborn and life-long abnormality of TGF-β signaling in vasculature, these diseases result in a tendency toward hemorrhage in capillaries that is due to vulnerability of the vascular structure. These observations suggest that use of TβR-I inhibitor at a dose corresponding to that in mice in our study may have similar effects in humans. However, the inhibition of TGF-β signaling is only transient in our method, because of the use of small-molecule inhibitor, and the effects of TβR-I inhibitor may thus be far less severe than the phenotypes observed in hereditary hemorrhagic telangiectasia.

The changes in tumor neovasculature induced by TβR-I inhibitor resulted in enhanced extravasation of molecules, although in a molecular-size dependent manner. Accumulation of 2-MDa dextran with a 50-nm hydrodynamic diameter, Doxil with a 108-nm diameter, and micelle ADR with a 65-nm diameter was enhanced by TβR-I inhibitor in the present study, although accumulation of small-molecule agents, including ADR (MW 543.52) and BrdU (MW 307.10) (M.R.K., unpublished data), was not significantly enhanced. Dreher *et al.* (24) recently reported the molecular-size-dependency of intratumoral drug distribution, using a xenograft model of FaDu cells derived from human hypopharyngeal squamous cell carcinoma. They used several dextrans with molecular sizes ranging from 3.3 kDa to 2 MDa, with estimated hydrodynamic diameters of 3.5 nm to 50 nm, respectively. Dextran molecules of 3.3 kDa and 10 kDa, the smallest ones tested, were found to penetrate deeply and homogeneously into tumor tissue, although they remained in tumor tissue only transiently, for far less than 30 min. However, larger dextran of 2 MDa with a diameter of 50 nm, which we also used in the present study, for the most part remained in the vasculature in cancer tissue and reached only an ≈5-μm distance from the vessel wall at 30 min after injection. Although the histological characteristics of their model, which were not described in their report, may differ from those of the cancer models used in our study, the distribution of 2-MDa dextran observed by Dreher *et al.* agrees with that obtained without TβR-I inhibitor in the BxPC3 xenografts observed in the present study (Fig. 3). TβR-I

inhibitor could thus enhance the accumulation of macromolecules with hydrodynamic diameters of >50 nm, common sizes for nanocarriers, in cancers other than those used in the present study. However, the range of sizes of macromolecules and histological patterns of cancer for which use of TβR-I inhibitor can exhibit enhancing effects remains to be determined.

In conclusion, we have proposed here a use of small-molecule TβR-I inhibitor at a low dose to enhance EPR effect in intractable solid cancers. This method could be a breakthrough in chemotherapy by using nanocarriers in these cancers. Because low-dose TβR-I inhibitor does not affect cancer cells, it may reduce the potential side effects of TGF-β inhibitors, and its enhancing effect is independent of the reactivity of cancer cells to TGF-β signaling. Use of TGF-β inhibitors may thus enable reduction of the systemic doses of nanocarriers and thereby decrease the adverse effects of anticancer drugs.

Methods

TGF-β Inhibitors, Anticancer Drugs, and Antibodies. TβR-I inhibitor was purchased from Calbiochem (San Diego, CA) (LY364947; catalog no. 616451). ADR was obtained from Nippon Kayaku (Tokyo, Japan) and purchased from Kyowa Hakko (Tokyo, Japan). Doxil was purchased from Alza (Mountain View, CA). Micelle ADR was prepared as reported (22) (see *SI Materials and Methods* for detailed information). The antibodies to PE-CAM-1 and VE-cadherin were from BD PharMingen (San Diego, CA), those to neuroglycan 2 and collagen IV were from Chemicon (Temecula, CA), and that to SMA was from Sigma–Aldrich (St. Louis, MO). The anti-phospho-Smad2 antibody was a gift from A. Moustakas and C.-H. Heldin (Ludwig Institute for Cancer Research, Uppsala, Sweden).

Cancer Cell Lines and Animals. BxPC3, MiaPaCa-2, and Panc-1 human pancreatic adenocarcinoma cell lines were obtained from the American Type Culture Collection (Manassas, VA). The OCUM-2MLN human diffuse-type gastric cancer cell line was previously established (27). BxPC3 cells were grown in RPMI medium 1640 supplemented with 10% FBS. MiaPaCa-2, Panc-1, and OCUM-2MLN cells were grown in DMEM with 10% FBS. BALB/c nude mice, 5–6 weeks of age, were obtained from CLEA Japan (Tokyo, Japan), Sankyo Laboratory (Tokyo, Japan), and Charles River Laboratories, (Tokyo, Japan). All animal experimental protocols were performed in accordance with the policies of the Animal Ethics Committee of the University of Tokyo.

Cancer Models. The effects of anticancer drugs were assessed by s.c. implantation of cancer cells into nude mice, and by orthotopic inoculation of OCUM-2MLN cells into the gastric walls of nude mice. A total of 5 × 10⁶ cells in 100 μl of PBS for the xenograft models and the same number in 50 μl of PBS for the orthotopic model were injected into male nude mice and allowed to grow for 2–3 weeks to reach proliferative phase, before initiation of drug administration. For growth-curve studies, the day of initiation of drug administration was considered day 0, and TβR-I inhibitor, dissolved to 5 mg/ml in DMSO and diluted by 100 μl of PBS, or the vehicle control, was injected i.p. at 1 mg/kg on day 0 only in the experiment shown in Fig. 4A and on days 0, 2, 4, 6, and 8 in other experiments. Doxil, micelle ADR, and free ADR at 8 mg/kg, or normal saline as vehicle control, were also administered i.v. in 200 μl/vol via the tail vein on day 0 (Fig. 4A). In other experiments, micelle ADR at 16 mg/kg, free ADR at 8 mg/kg, or normal saline was also administered i.v. on days 0, 4, and 8. There were five mice per group per cell line. The doses of ADR and Doxil were determined based on the lethal doses in mice (22, 26). For biodistribution studies, three mice per group per cell line were treated with 8 mg/kg Doxil, micelle

ADR, or free ADR i.v., with and without TβR-I inhibitor at 1 mg/kg i.p. The mice were examined 24 h after injection.

Quantification in Tumor Models. Xenograft tumors were measured externally every second day until day 16, and tumor volume was approximated by using the equation vol $= (a \times b^2)/2$, where vol is volume, a the length of the major axis, and b is the length of the minor axis. Relative tumor volume was calculated by dividing tumor volume by that on day 0 (the day of initiation of treatment), where actual estimated volumes of xenografted tumors in mm^3 at initiation of drug administration were as follows (mean ± standard error): BxPC3 (in Fig. 4A), 76.4 ± 7.0; BxPC3 (in Fig. 4B), 74.4 ± 3.3; MiaPaCa-2, 221.2 ± 12.7; and Panc-1, 242.16 ± 24.5. For orthotopic OCUM-2MLN tumors, the area of the primary focus on the gastric wall was measured in Adobe Photoshop software, by opening the abdomen before initiation of treatment and at the end of the observation period. Relative tumor area was calculated by dividing tumor area by that on the day of initiation of treatment. The results were further analyzed statistically by the multivariate ANOVA test, using JMP6 software (SAS Institute, Raleigh, NC).

Histology and Immunohistochemistry. The excised samples were either directly frozen in dry-iced acetone for immunohistochemistry, or fixed overnight in 4% paraformaldehyde and then paraffin-embedded to prepare them for H&E or AZAN staining. Frozen samples were further sectioned at 10-μm thickness in a cryostat, briefly fixed with 10% formalin, and then incubated with primary and secondary antibodies. TOTO-3 for nuclear staining, Alexa488-, Alexa594-, and Alexa647-conjugated secondary antibodies, anti-rat and rabbit IgGs, Zenon labeling kit anti-rabbit and mouse IgG, and FITC-conjugated dextran (MW 2×10^6) were purchased from Invitrogen Molecular Probes (Eugene, OR). Samples were observed by using a Zeiss (Thornwood, NY) LSM510 Meta confocal microscope for immunohistochemistry, and an Olympus (Tokyo, Japan) AX80 microscope for H&E and AZAN staining.

Biodistribution. Xenografts were inoculated s.c. in nude mice and allowed to grow for 2–3 weeks before drug administration. We then injected TβR-I inhibitor at 1 mg/kg i.p. together with i.v. administration of Doxil, micelle ADR, or free ADR at 8 mg/kg. The tumors or organs were excised 24 h after injection of drugs, and frozen in dry-iced acetone to obtain fluorescence images or weighed and mixed with daunorubicin commensurate with the sample weight as an internal control and then frozen to prepare them for measurement by HPLC. The HPLC method used for analyses is described in ref. 22. To obtain fluorescence images, we performed cryostat sectioning of the frozen samples and washed the sections twice briefly with PBS but did not fix them to avoid elution of ADR. The samples were then observed with a Zeiss confocal microscope, using an excitation laser at 488 nm and a detection filter for the infrared region.

1. Muggia FM (2001) *Curr Oncol Rep* 3:156–162.
2. Ferrari M (2005) *Nat Rev Cancer* 5:161–171.
3. Hassan M, Little RF, Vogel A, Aleman K, Wyvill K, Yarchoan R, Gandjbakhche AH (2004) *Technol Cancer Res Treat* 3:451–457.
4. Emoto M, Udo T, Obama H, Eguchi F, Hachisuga T, Kawarabayashi T (1998) *Gynecol Oncol* 70:351–357.
5. Duncan R (2006) *Nat Rev Cancer* 6:688–701.
6. Kataoka K, Harada A, Nagasaki Y (2001) *Adv Drug Deliv Rev* 47:113–131.
7. Hamaguchi T, Matsumura Y, Suzuki M, Shimizu K, Goda R, Nakamura I, Nakatomi I, Yokoyama M, Kataoka K, Kakizoe T (2005) *Br J Cancer* 92:1240–1246.
8. Nishiyama N, Okazaki S, Cabral H, Miyamoto M, Kato Y, Sugiyama Y, Nishio K, Matsumura Y, Kataoka K (2003) *Cancer Res* 63:8977–8983.
9. MacKenzie MJ (2004) *Lancet Oncol* 5:541–549.
10. Fuchs CS, Mayer RJ (1995) *N Engl J Med* 333:32–41.
11. Burris HA, III, Moore MJ, Andersen J, Green MR, Rothenberg ML, Modiano MR, Cripps MC, Portenoy RK, Storniolo AM, Tarassoff P, et al. (1997) *J Clin Oncol* 15:2403–2413.
12. Watanabe N, Tsuji N, Tsuji Y, Sasaki H, Okamoto T, Akiyama S, Kobayashi D, Sato T, Yamauchi N, Niitsu Y (1996) *Pancreas* 13:395–400.
13. Matsumura Y, Maeda H (1986) *Cancer Res* 46:6387–6392.
14. Maeda H, Matsumura Y (1989) *Crit Rev Ther Drug Carrier Syst* 6:193–210.
15. Sofuni A, Iijima H, Moriyasu F, Nakayama D, Shimizu M, Nakamura K, Itokawa F, Itoi T (2005) *J Gastroenterol* 40:518–525.
16. Takahashi Y, Cleary KR, Mai M, Kitadai Y, Bucana CD, Ellis LM (1996) *Clin Cancer Res* 2:1679–1684.
17. Roberts AB, Wakefield LM (2003) *Proc Natl Acad Sci USA* 100:8621–8623.
18. Feng XH, Derynck R (2005) *Annu Rev Cell Dev Biol* 21:659–693.
19. Bandyopadhyay A, Agyin JK, Wang L, Tang Y, Lei X, Story BM, Cornell JE, Pollock BH, Mundy GR, Sun L-Z (2006) *Cancer Res* 66:6714–6721.
20. Yingling JM, Blanchard KL, Sawyer JS (2004) *Nat Rev Drug Discov* 3:1011–1022.

21. Sawyer JS, Anderson BD, Beight DW, Campbell RM, Jones ML, Herron DK, Lampe JW, McCowan JR, McMillen WT, Mort N, et al. (2003) *J Med Chem* 46:3953–3956.
22. Bae Y, Nishiyama N, Fukushima S, Koyama H, Matsumura Y, Kataoka K (2005) *Bioconjug Chem* 16:122–130.
23. Kano MR, Morishita Y, Iwata C, Iwasaka S, Watabe T, Ouchi Y, Miyazono K, Miyazawa K (2005) *J Cell Sci* 118:3759–3768.
24. Dreher MR, Liu W, Michelich CR, Dewhirst MW, Yuan F, Chilkoti A (2006) *J Natl Cancer Inst* 98:335–344.
25. McDonald DM, Choyke PL (2003) *Nat Med* 9:713–725.
26. Gabizon A, Tzemach D, Mak L, Bronstein M, Horowitz AT (2002) *J Drug Target* 10:539–548.
27. Yashiro M, Chung YS, Nishimura S, Inoue T, Sowa M (1996) *Clin Exp Metastasis* 14:43–54.
28. Li DY, Sorensen LK, Brooke BS, Urness LD, Davis EC, Taylor DG, Boak BB, Wendel DP (1999) *Science* 284:1534–1537.
29. Arthur HM, Ure J, Smith AJ, Renforth G, Wilson DI, Torsney E, Charlton R, Parums DV, Jowett T, Marchuk DA, et al. (2000) *Dev Biol* 217:42–53.
30. Oh SP, Seki T, Goss KA, Imamura T, Yi Y, Donahoe PK, Li L, Miyazono K, ten Dijke P, Kim S, et al. (2000) *Proc Natl Acad Sci USA* 97:2626–2631.
31. Urness LD, Sorensen LK, Li DY (2000) *Nat Genet* 26:328–331.
32. Larsson J, Goumans MJ, Sjostrand LJ, van Rooijen MA, Ward D, Leveen P, Xu X, ten Dijke P, Mummery CL, Karlsson S (2001) *EMBO J* 20:1663–1673.
33. Watabe T, Nishihara A, Mishima K, Yamashita J, Shimizu K, Miyazawa K, Nishikawa S-I, Miyazono K (2003) *J Cell Biol* 163:1303–1311.
34. Hirschi KK, Rohovsky SA, D'Amore PA (1998) *J Cell Biol* 141:805–814.
35. Lebrin F, Deckers M, Bertolino P, ten Dijke P (2005) *Cardiovasc Res* 65:599–608.
36. Fernandez-L A, Sanz-Rodriguez F, Blanco FJ, Bernabeu C, Botella LM (2006) *Clin Med Res* 4:66–78.

Inhibition of Cyclooxygenase-2 Suppresses Lymph Node Metastasis via Reduction of Lymphangiogenesis

Caname Iwata,[1,2] Mitsunobu R. Kano,[1,3] Akiyoshi Komuro,[1] Masako Oka,[1] Kunihiko Kiyono,[1] Erik Johansson,[1] Yasuyuki Morishita,[1] Masakazu Yashiro,[4] Kosei Hirakawa,[4] Michio Kaminishi,[2] and Kohei Miyazono[1,3]

Departments of [1]Molecular Pathology and [2]Gastrointestinal Surgery, Graduate School of Medicine, [3]Center for NanoBio Integration, University of Tokyo, Tokyo, Japan and [4]Department of Surgical Oncology, Medical School, Osaka City University, Osaka, Japan

Abstract

Cyclooxygenase-2 (COX-2) inhibitor has been reported to suppress tumor progression. However, it is unclear whether this inhibitor can also prevent lymphatic metastasis. To determine the effects of COX-2 inhibitor on lymphatic metastasis, etodolac, a COX-2 inhibitor, was given p.o. to mice bearing orthotopic xenografts or with carcinomatous peritonitis induced with a highly metastatic human diffuse-type gastric carcinoma cell line, OCUM-2MLN. Tumor lymphangiogenesis was significantly decreased in etodolac-treated mice compared with control mice. Consistent with this decrease in lymphangiogenesis, the total weight of metastatic lymph nodes was less in etodolac-treated mice than in control mice. Immunohistochemical analysis revealed that the major source of vascular endothelial growth factor-C (VEGF-C) and VEGF-D was F4/80-positive macrophages in our models. The mRNA levels of VEGF-C in mouse macrophage-like RAW264.7 cells, as well as those in tumor tissues, were suppressed by etodolac. The growth of human dermal lymphatic microvascular endothelial cells was also suppressed by etodolac. Supporting these findings, etodolac also inhibited lymphangiogenesis in a model of chronic aseptic peritonitis, suggesting that COX-2 can enhance lymphangiogenesis in the absence of cancer cells. Our findings suggest that COX-2 inhibitor may be useful for prophylaxis of lymph node metastasis by reducing macrophage-mediated tumor lymphangiogenesis. [Cancer Res 2007;67(21):10181–9]

Introduction

Lymph node metastasis is a common occurrence in cancer, and lymphatic vessels serve as an important route for the spread of cancer cells (1, 2). Lymphatic metastasis was previously believed to be a passive process in which detached cancer cells reach lymph nodes through preexisting local lymphatic vessels (3). However, recent studies have suggested that lymphangiogenesis actively contributes to metastasis based on the observations that lymphatic vessel density is correlated with the extent of lymph node metastasis and/or unfavorable prognosis of certain cancers (2, 4, 5). Moreover, some animal tumor models have revealed that

expression of lymphangiogenic growth factors leads to formation of lymphatic vessels and that lymphangiogenesis is accompanied by enhanced lymphatic metastasis (2). These findings strongly suggest that lymphatic metastasis can be blocked by inhibition of tumor lymphangiogenesis (1, 6, 7).

The best studied lymphangiogenic signaling system is the vascular endothelial growth factor-C (VEGF-C)/VEGF-D and VEGF receptor 3 (VEGF-R3) signaling axis, which has been shown to play a central role in lymphangiogenesis in animal models (1, 2, 4). Elevated expression of VEGF-C or VEGF-D has been observed in many human cancers (2, 4). A number of studies have shown that levels of expression of VEGF-C in primary tumor correlate with lymphatic vessel invasion and/or lymph node metastasis (2, 4, 8), although the correlation between VEGF-D and metastasis is currently unclear (4, 9). These ligands are thought to be secreted from tumor cells; in addition, macrophages in the peritumoral stroma (i.e., tumor-associated macrophages) have also been reported to produce VEGF-C and VEGF-D in certain cancers and to induce lymphangiogenesis (10). The contribution of inflammatory cells to lymphangiogenesis has also been shown in mouse models of inflammation (11, 12).

Epidemiologic studies have shown that regular intake of nonsteroidal antiinflammatory drugs (NSAID), prototypic inhibitors of cyclooxygenase (COX), such as aspirin, can reduce the risk of development of some cancers (13). In addition, overexpression of COX-2, which is induced by both inflammatory and mitogenic stimuli, is commonly found in many cancers (14–16), suggesting that COX-2 contributes to the process of carcinogenesis. Direct molecular evidence that COX-2 contributes to carcinogenesis has been obtained from studies in animals engineered to be deficient in expression of the COX-2 gene (17) or treated with COX-2 selective inhibitors (18). Thus far, several mechanisms by which COX-2 contributes to progression of cancer have been reported, including stimulation of proliferation and inhibition of apoptosis of cancer cells, stimulation of cancer cell invasion and angiogenesis, and suppression of immune responses (14, 19).

The major role of COX-2 in angiogenesis is thought to be induction of the synthesis of prostanoids, which then stimulate the secretion of proangiogenic factors, including VEGF-A and fibroblast growth factor-2, from cancer cells and/or stromal fibroblasts (20, 21). In addition, COX-2 stimulates the proliferation (22), migration, and tube formation of vascular endothelial cells (20). Several clinical studies have indeed shown a correlation between level of COX-2 expression and extent of angiogenesis in cancer (23).

In contrast to the effect of COX-2 on angiogenesis, that on lymphangiogenesis remains poorly understood, although correlations between COX-2 expression and lymphangiogenesis or lymph node metastasis have been reported for several human cancers

(24–28). To examine whether COX-2 is involved in lymphatic metastasis, we evaluated the effects of treatment with a COX-2 selective inhibitor, etodolac (29, 30), on tumor lymphangiogenesis and extent of lymph node metastasis using a highly metastatic human diffuse-type gastric carcinoma cell line, OCUM-2MLN (31). We also examined the effects of etodolac on lymphangiogenesis in two other animal models, i.e., a model of carcinomatous peritonitis and one of chronic aseptic peritonitis. Our findings suggest that etodolac has antilymphangiogenic activity *in vivo* and that inhibition of COX-2 could suppress tumor lymphangiogenesis and lymph node metastasis.

Materials and Methods

Animals and cells. Immunodeficient BALB/c nu/nu mice at 4 to 5 weeks of age, obtained from Charles River Laboratories, were used for the model of lymph node metastasis and a model of carcinomatous peritonitis. Specific pathogen-free BALB/c mice at 4 to 5 weeks of age, obtained from Sankyo Laboratory, were used for a model of chronic aseptic peritonitis. Mice were treated in accordance with the policies of the Animal Ethics Committee of the University of Tokyo. OCUM-2MLN, a human diffuse-type gastric carcinoma cell line with a high rate of metastasis to lymph nodes, was previously established (31). RAW264.7, a mouse macrophage-like cell line, was a kind gift from Dr. Tadashi Muroi (NIH Sciences). Human dermal lymphatic microvascular endothelial cells (HDLEC) were obtained from Cambrex.

Model of lymph node metastasis. We used a lentiviral vector (a kind gift from Dr. Hiroyuki Miyoshi, RIKEN; ref. 32) to express the *green fluorescent protein (GFP)* gene stably in OCUM-2MLN. A total of 5×10^6 cells in 50 µL of PBS were subserosally inoculated into the gastric walls of BALB/c nu/nu mice as previously described (31) under deep inhalation anesthesia with ether. Four weeks after inoculation, the mice were sacrificed for evaluation. Etodolac (500 ppm in food; obtained from Nippon Shinyaku) or vehicle control was given p.o. throughout the experimental period from the inoculation of cancer cells until evaluation ($n = 7$ mice for each group). The experiment was repeated thrice.

Spread of cancer cells from the site of inoculation in the stomach was observed with a VB-G25 fluorescence stereomicroscope (Keyence). The captured fluorescence images and bright-field images were merged using Adobe Photoshop software (Adobe Systems). All GFP-positive, i.e., metastatic, lymph nodes were collected, and the total weight of these lymph nodes was measured. Stomachs were excised, fixed for 1 h in 10% neutral buffered formalin at room temperature, washed overnight in PBS containing 10% sucrose at 4°C, embedded in optimal cutting temperature compound (Tissue-Tek, Sakura Finetek), and snapped frozen in dry-iced acetone for immunohistochemical examination.

To visualize the lymphatic vessels in normal gastric wall, we injected India ink into the gastric wall of anesthetized control mice and immediately observed the draining lymphatic vessels by stereomicroscope.

Model of carcinomatous peritonitis. We i.p. injected OCUM-2MLN cells (5×10^6) into BALB/c nu/nu mice to induce carcinomatous peritonitis. The mice were sacrificed 2 weeks after inoculation and were evaluated. Etodolac (500 ppm in food) or vehicle control was given p.o. throughout the experimental period from injection of cancer cells until evaluation ($n = 5$ for each group). Diaphragms with disseminated tumor cells were excised, carefully extended, fixed for 30 min in 10% neutral buffered formalin at room temperature, and washed overnight in PBS containing 10% sucrose at 4°C. These diaphragms were embedded in optimal cutting temperature compound and snapped frozen in dry-iced acetone for immunohistochemical study or whole-mount immunostained. The experiment was repeated twice.

To visualize the lymphatic vessels in normal diaphragm, we i.p. injected India ink to control mice and observed the lymphatic vessels filled with ink in the diaphragms 20 min later.

Model of chronic aseptic peritonitis. We i.p. injected 2 mL of 3% thioglycollate medium (BBL thioglycollate medium, BD Biosciences) into BALB/c mice thrice a week for 2 weeks to induce peritonitis. Etodolac (500 ppm in food) or vehicle control was given p.o. during the same period ($n = 5$ for each group). The mice were then sacrificed, and their diaphragms excised and prepared for H&E staining and immunostaining as described above. The experiment was repeated twice.

Immunohistochemistry. Whole mounts of diaphragms and 20-µm cryostat sections of postfixed frozen samples were stained with one or more primary antibodies. We used the following antibodies for immunostaining. For staining of lymphatic vessels, rabbit polyclonal antibody to LYVE-1 (1:200 dilution; Abcam), rat monoclonal antibody to mouse LYVE-1 (1:100 dilution; a kind gift from Drs. Yuichi Oike and Toshio Suda, Keio University), or rabbit polyclonal antibody to Prox1 (1:200 dilution; Chemicon) was used. Rat monoclonal antibody to mouse platelet/ endothelial cell adhesion molecule 1 (PECAM-1; 1:200 dilution; BD PharMingen) was used for staining of blood vessels. For staining of VEGF-C and VEGF-D, goat polyclonal antibody to VEGF-C (C-20; 1:50 dilution, Santa Cruz Technology), and rabbit polyclonal antibody to VEGF-D (H-144; 1:50 dilution, Santa Cruz Technology) were used, respectively. Macrophages were immunostained with rat monoclonal antibody to F4/80 (1:20 dilution; Serotec) or rat monoclonal antibody to mouse CD11b (1:200 dilution; Chemicon). Dividing cells were stained with rabbit polyclonal antibody to Ki-67 (1:1,000 dilution; Novo Castra). COX-2 was stained with affinity-purified rabbit polyclonal antibody to COX-2 (1:100 dilution; Cayman Chemical). Subsequently, specimens were incubated with corresponding secondary antibodies labeled with Alexa Fluors 488, 594, or 647 (Invitrogen-Molecular Probes) at 1:200 dilution. Cell nuclei were counterstained with 20 µmol/L TOTO-3 (Invitrogen-Molecular Probes). In control experiments, the primary antibody was omitted. Specimens were examined with a LSM 510 META confocal microscope (Carl Zeiss) or a fluorescence stereomicroscope.

Morphometric analysis. In the model of lymph node metastasis, we double-stained tumor sections for LYVE-1 and PECAM-1 to examine lymphatic and blood vessel densities. For each tumor section, five hotspots (i.e., fields with the highest vascular density) in tumor areas were evaluated at magnification of 200×. Digital images of LYVE-1–positive lymphatic vessels and highly PECAM-1–positive blood vessels were captured. Area densities (percentage of total tissue area) of lymphatic vessels or blood vessels were then calculated using ImageJ software (NIH).

In the model of carcinomatous peritonitis, whole-mount diaphragms stained for LYVE-1 were evaluated from the pleural side. Lymphatic sprouts, defined as tapered projections, were counted at magnification of 100× in 10 microscopic fields per diaphragm.

In the model of chronic aseptic peritonitis, whole-mount diaphragms stained for LYVE-1 and CD11b were evaluated from the peritoneal side. Inflammatory plaques, defined as accumulations of inflammatory cells, especially of macrophages, had formed on the peritoneal surface of the diaphragm. For each diaphragm, 10 microscopic fields in inflammatory plaques were evaluated at magnification of 200×. Digital images of LYVE-1–positive lymphatic vessels were captured, and the area density of lymphatic vessel was calculated using ImageJ software.

RNA isolation and quantitative reverse transcription–PCR. Gastric walls with or without tumor were excised from mice, immersed in RNAlater (Qiagen), embedded in optimal cutting temperature compound, and snapped frozen. Total RNAs were extracted from tissue sections using the RNeasy micro kit (Qiagen). Total RNAs from RAW264.7 and HDLECs were extracted using the RNeasy mini kit (Qiagen). First-strand cDNAs were synthesized using the Quantitect reverse transcription kit (Qiagen) with random hexamer primers. Quantitative real-time reverse transcription–PCR (RT-PCR) analysis was done using the 7500 Fast Real-Time PCR system (Applied Biosystems). The primer sequences used are given in Supplementary Table S1.

Cell growth assay. Cell growth was determined with a WST-8 assay kit (Nacalai Tesque). Briefly, HDLECs (1×10^3 cells per well) or OCUM-2MLN (7.5×10^2 cells per well) in 96-well plates were incubated overnight. Thereafter, the medium was replaced with a new medium containing etodolac and/or lipopolysaccharide (LPS; O111:B4; Sigma-Aldrich). After 24 to 96 h of incubation, the WST-8 reagent was added to the culture. After

2 h of incubation, absorbance at 450 nm was measured with a microplate reader (Bio-Rad).

Statistical analysis. Statistical analysis was carried out using Excel software (Microsoft). Results were compared by Student's t test and expressed as mean values with SE. Differences were considered statistically significant at $P < 0.05$. All statistical tests were two-sided. Effects of etodolac on the growth of OCUM-2MLN were evaluated by multivariate ANOVA testing using JMP software (SAS Institute).

Results

Spread of cancer cells via lymphatic vessels in a murine model of lymph node metastasis of gastric cancer. To determine lymph node metastasis *in vivo*, we used an animal model of human metastatic gastric carcinoma, in which OCUM-2MLN cells expressing GFP were inoculated orthotopically into the gastric wall of BALB/c nu/nu mice. Examination by fluorescence stereomicroscope 4 weeks after inoculation revealed that the cancer cells had metastasized from the site of inoculation into the regional lymph nodes. Using this model, we examined tumor

lymphangiogenesis and spread of cancer cells through the lymphatic vessels. The cancer cells in this model exhibited invasion into peritumoral lymphatic vessels and spread along lymphatic vessels in the gastric wall toward the regional lymph nodes (Fig. 1A). Visualization by intravital injection of India ink into the gastric wall of control mice (Supplementary Fig. S1) revealed that the sizes and numbers of the lymphatic vessels were dramatically increased in the mice inoculated with gastric cancer cells (Fig. 1A) compared with those in control mice. To confirm the increase in lymphatic vessels in the mice bearing cancer cells, we double-stained the sections of the gastric wall of the mice using LYVE-1, a specific lymphatic vessel marker, and Ki-67, a marker of cell proliferation. Some dividing lymphatic endothelial cells stained by both LYVE-1 and Ki-67 were observed in the gastric wall of the tumor-bearing mice (Fig. 1B), demonstrating induction of lymphangiogenesis in this model.

Suppression of lymphangiogenesis and lymph node metastasis by etodolac in the model of lymph node metastasis. We examined whether etodolac, a COX-2 inhibitor, inhibits
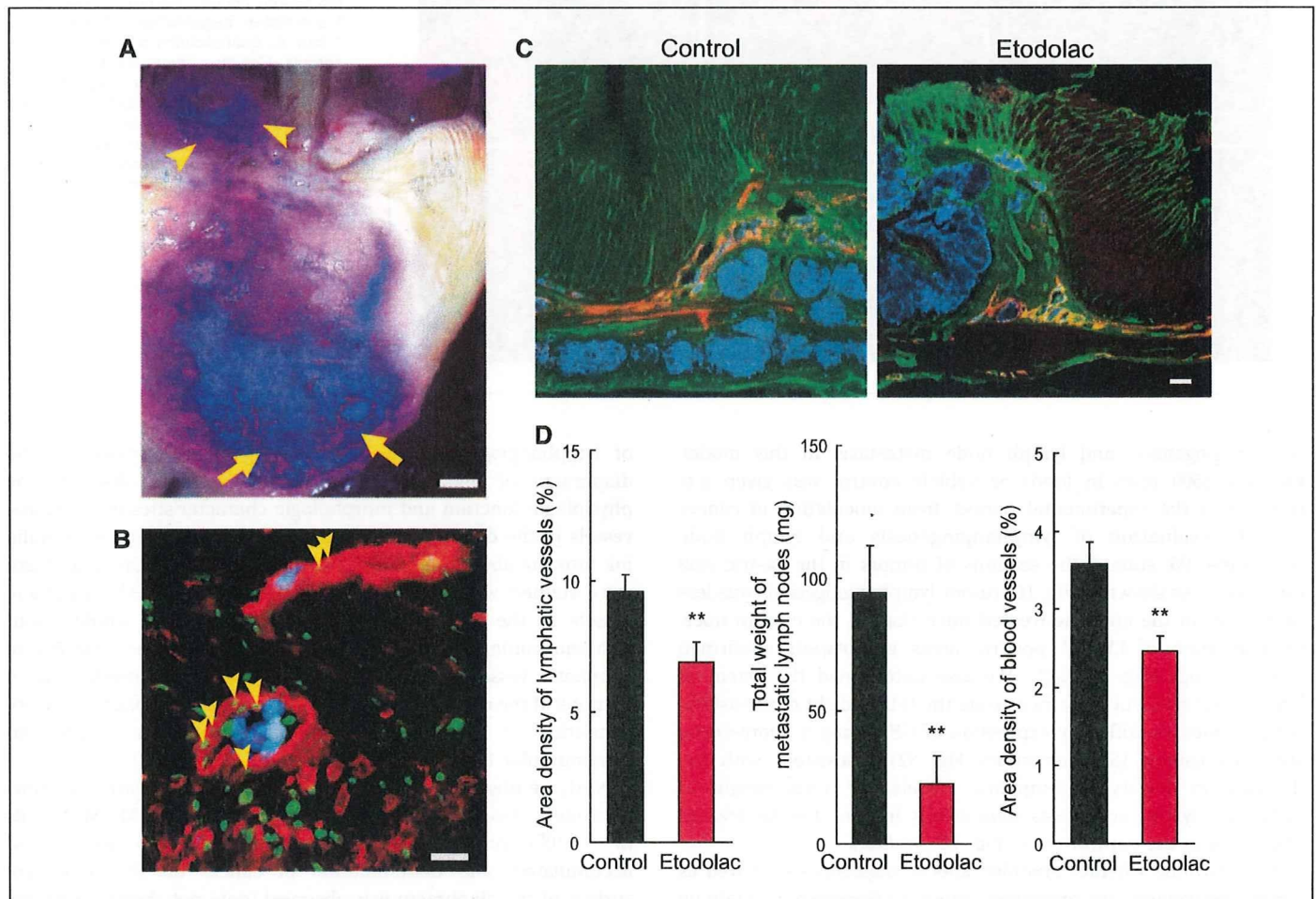

Figure 1. Effects of etodolac on a murine model of lymph node metastasis of gastric carcinoma. *A,* spread of GFP-expressing OCUM-2MLN cells 4 wk after inoculation into gastric wall of BALB/c nu/nu mouse. GFP-positive cancer cells (*purple*) which have invaded peritumoral lymphatic vessels in the gastric wall and metastasized to regional lymph nodes (*arrowheads*). *Arrows,* orthotopically inoculated OCUM-2MLN tumor. *Scale bar,* 1 mm. *B,* cross-section of gastric wall with GFP-positive cancer cells (*blue*), stained for lymphatic vessels (anti–LYVE-1; *red*) and dividing nuclei (anti–Ki-67; *green*). *Arrowheads,* lymphatic endothelial cells positive for Ki-67. *Scale bar,* 20 μm. *C,* orthotopic GFP-positive OCUM-2MLN (*blue*) tumor in control mice or in etodolac-treated mice, stained for lymphatic vessels (anti–LYVE-1; *red*) and blood vessels (anti–PECAM-1; *green*). *Scale bar,* 50 μm. *D, left,* quantification of tumor lymphatic vessels. Columns, mean area density of LYVE-1-positive pixels per microscopic field; *bars,* SE (data from one section per tumor, with 10 images per section). **, $P = 0.008$, two-sided Student's t test. *Middle,* total weights of metastatic lymph nodes from control mice and etodolac-treated mice. *Columns,* mean; *bars,* with SE. **, $P = 0.006$. *Right,* quantification of tumor blood vessels. *Columns,* mean area density of pixels highly positive for PECAM-1 per microscopic field; *bars,* SE. **, $P = 0.002$.
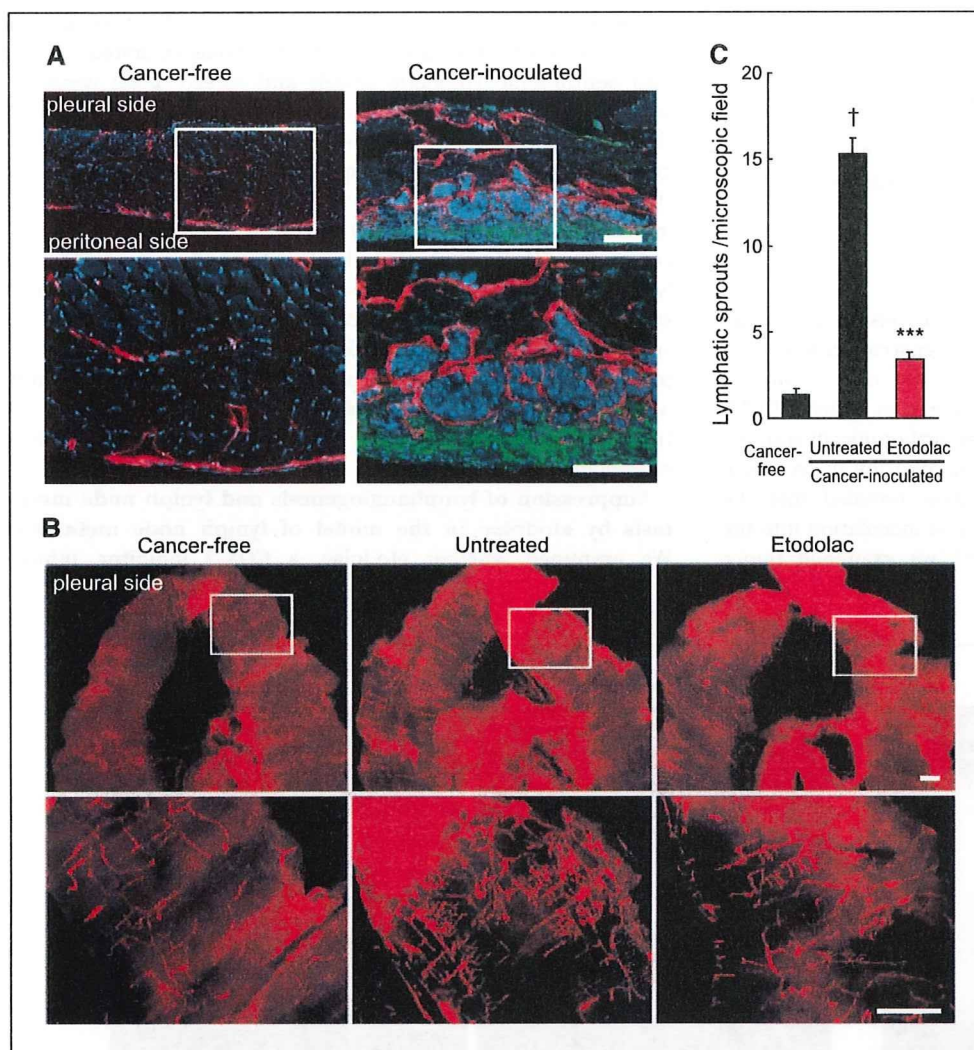
Figure 2. Effects of etodolac on lymphangiogenesis in the model of carcinomatous peritonitis. *A,* lymphatic vessels in the diaphragm in normal mice and those with carcinomatous peritonitis. Immunostaining of lymphatic vessels (anti–LYVE-1, *red*), macrophages (anti-F4/80, *green*), and nuclei (*blue*) in parasagittal sections of the diaphragm from cancer-free mice and those with carcinomatous peritonitis induced by OCUM-2MLN. *Top,* middle magnification; *bottom,* the boxed areas in the top in higher magnification. *Scale bars,* 100 µm. *B,* whole-mount immunostaining for lymphatic vessels (anti–LYVE-1, *red*) of diaphragms from cancer-free mice and those with carcinomatous peritonitis treated with vehicle control or etodolac. *Top,* images of the entire diaphragm at low power; *bottom,* the boxed areas in the top in higher magnifications. *Scale bars,* 1 mm. *C,* quantification of lymphatic sprouts. *Columns,* mean number of lymphatic sprouts per microscopic field; *bars,* SE. $n = 5$ mice for each group and 10 fields per mouse; cancer-inoculated control mice versus cancer-free mice: †, $P < 0.001$; etodolac-treated mice versus cancer-inoculated control mice: ***, $P < 0.001$.

lymphangiogenesis and lymph node metastasis in this model. Etodolac (500 ppm in food) or vehicle control was given p.o. throughout the experimental period, from inoculation of cancer cells to evaluation of lymphangiogenesis and lymph node metastasis. We stained the sections of tumors in the gastric wall for LYVE-1. As shown in Fig. 1*C,* tumor lymphangiogenesis was less prominent in the etodolac-treated mice than in the control mice. Quantification of LYVE-1–positive areas in hotspots confirmed these findings (Fig. 1*D, left*). We also determined the extent of lymph node metastasis by measuring the total weight of metastatic lymph nodes identified by expression of GFP using a fluorescence stereomicroscope (Supplementary Fig. S2). Consistent with the decrease in density of lymphatic vessels, the total weight of metastatic lymph nodes was significantly less in etodolac-treated mice than in the control mice (Fig. 1*D, middle*).

To determine whether etodolac affects angiogenesis, as well as lymphangiogenesis, we examined tumor angiogenesis by staining sections of tumors for PECAM-1. The relative area occupied by vessels strongly positive for PECAM-1 was significantly decreased in the etodolac-treated mice compared with the control mice (Fig. 1*D, right*).

Lymphatic vessels in the diaphragm in normal mice and those with carcinomatous peritonitis. To evaluate tumor lymphangiogenesis in another fashion, we established a new model

of lymphangiogenesis, in which the lymphatic vessels of the diaphragm of mice can be observed. We first observed the physiologic function and morphologic characteristics of lymphatic vessels in the diaphragm. Only 20 min after the injection of India ink into the abdominal cavity, lymphatic vessels in the diaphragm were stained with the ink (Supplementary Fig. S3*A*). Lymphatic vessels in the diaphragm were also observed by whole-mount immunostaining for LYVE-1 and Prox1 as specific markers of lymphatic vessels (Supplementary Fig. S3*B*). Immunostaining of sections of the diaphragm for LYVE-1 revealed a lymphatic network consisting of lymphatic lacunae on the peritoneal side and intermuscular lymphatic vessels (Fig. 2*A, left*; ref. 33).

Next, we observed the diaphragms of mice with carcinomatous peritonitis. Two weeks after i.p. inoculation of OCUM-2MLN cells (5×10^6) into BALB/c nu/nu mice, cancerous ascites had accumulated, and dissemination of cancer on the peritoneal surface of the diaphragm was observed (data not shown). Sections of diaphragm revealed that these sites of dissemination consisted of cancer cells and F4/80-positive macrophages (Fig. 2*A, right*). The lymphatic vessels in the diaphragm were increased in both size and number. Outgrowths of the lymphatic vessels into the site of dissemination were also detected (Fig. 2*A*).

Suppression of lymphangiogenesis by etodolac in the model of carcinomatous peritonitis. As described above, lymphatic

vessels in the diaphragm can be evaluated not only by using tissue sections but also by using whole-mount samples. Using this model, we examined the effects of etodolac on tumor lymphangiogenesis. Etodolac or vehicle control was continuously given for 2 weeks from the time of inoculation of cancer cells to evaluation of lymphangiogenesis. We observed the lymphatic vessels in the diaphragm by whole-mount immunostaining for LYVE-1 from the pleural side. More sprouts were detected along lymphatic vessels over the entire diaphragm in the cancer-inoculated mice than in the cancer-free mice (Fig. 2B). However, the number of sprouts was less in the etodolac-treated mice than in the untreated mice (Fig. 2B). Quantification of lymphatic sprouts revealed significant reduction of lymphangiogenesis by treatment with etodolac (Fig. 2C).

Expression of VEGF-C/VEGF-D and COX-2 in tumor tissues. Macrophages have been suggested to be the major cellular sources of lymphangiogenic growth factors VEGF-C and VEGF-D (10–12). To determine whether macrophages are also the major source of these ligands in our model, we did immunohistochemical staining for macrophage marker F4/80 and VEGF-C or VEGF-D. In this model, many cells positive for VEGF-C (Fig. 3A, a) and VEGF-D (Fig. 3A, b) were F4/80-positive macrophages. Although certain cancer cells have also been reported to secrete these ligands, OCUM-2MLN cells were negative for VEGF-C (Fig. 3A, a) and VEGF-D (Fig. 3A, b) staining. These observations indicate that

macrophages are the major sources of lymphangiogenic growth factors in this model.

We further examined the expression of COX-2 to determine which cells are the targets of the COX-2 inhibitor etodolac. Some lymphatic endothelial cells (Fig. 3B) and OCUM-2MLN cells (Fig. 3C) expressed COX-2. As shown in Fig. 3C, some F4/80-positive macrophages were also COX-2 positive. These findings suggest that etodolac may act on several different types of cells in this model.

We also investigated the expression levels of mouse mRNA for VEGF-C (Fig. 3D, top) and VEGF-D (Fig. 3D, bottom) in the tumor tissues. Consistent with the results obtained by immunohisto-chemical analysis, mRNA level for VEGF-C and VEGF-D increased in the orthotopically inoculated tumors. In addition, the expression of VEGF-C, but not that of VEGF-D, was down-regulated after treatment with etodolac.

Effects of etodolac on macrophages, lymphatic endothelial cells, and cancer cells *in vitro*. Given the coexpression of COX-2 and VEGF-C or VEGF-D in macrophages, we hypothesized that etodolac suppresses the expression of VEGF-C and VEGF-D in macrophages. To test this hypothesis, we examined the mRNA levels of VEGF-C and VEGF-D in *in vitro*–cultured RAW264.7, a mouse macrophage-like cell line, by quantitative RT-PCR. The levels of expression of COX-2 (Fig. 4A) and VEGF-C (Fig. 4B) were dose-dependently up-regulated at 24 h after stimulation with LPS. The up-regulation of VEGF-C was, however, suppressed by
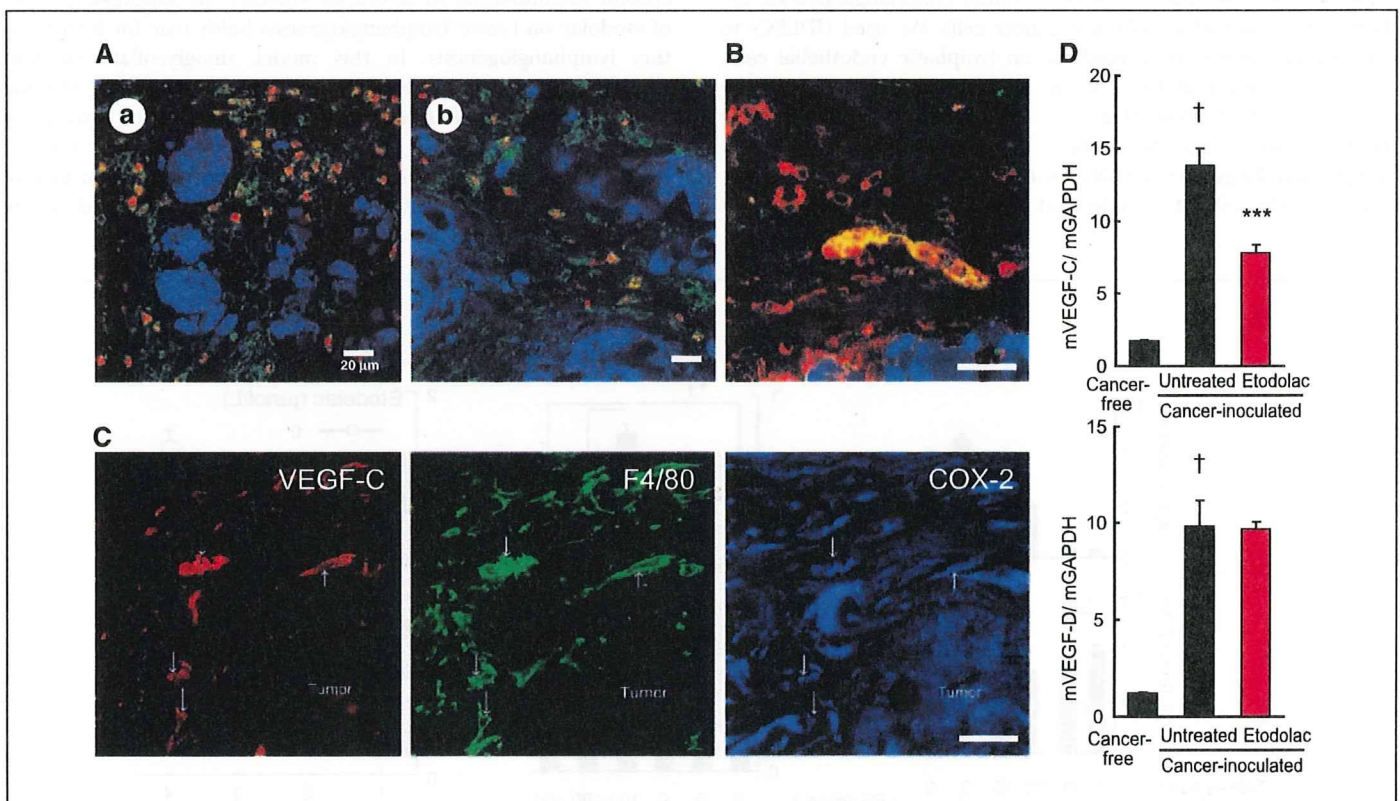

Figure 3. Expression of VEGF-C, VEGF-D, and COX-2 in tumor tissue. *A,* immunostaining of orthotopically inoculated tumors for VEGF-C (*a*) or VEGF-D (*b, red*), macrophages (anti-F4/80, *green*), and cancer cells (GFP, *blue*). Note that OCUM-2MLN cells themselves were negative for VEGF-C and VEGF-D. *Scale bar,* 20 μm. *B,* several lymphatic endothelial cells (anti–LYVE-1, *red*) in the GFP-expressing tumor (*blue*) overexpress COX-2 (*green*), suggesting that lymphatic endothelial cells in the tumor are also targets of etodolac. *Scale bar,* 20 μm. *C,* triple immunostaining for VEGF-C, F4/80, and COX-2 in the model of carcinomatous peritonitis showed colocalization of these markers. Most VEGF-C–positive cells were F4/80-positive macrophages, whereas some F4/80-positive macrophages were strongly positive for COX-2. *Arrows,* triple-positive cells. *Scale bar,* 20 μm. *D,* quantitative RT-PCR analysis of mouse mRNA for VEGF-C (*mVEGF-C, top*) and mouse mRNA for VEGF-D (*mVEGF-D*) expression (*bottom*). Both mouse mRNA for VEGF-C and VEGF-D increased in orthotopically inoculated tumors, and the expression of mouse mRNA for VEGF-C was down-regulated after 3 d of treatment with etodolac. *Columns,* mean; *bars,* SE. Cancer-inoculated control mice versus cancer-free mice: †, $P < 0.001$; etodolac-treated mice versus cancer-inoculated control mice: ***, $P < 0.001$.
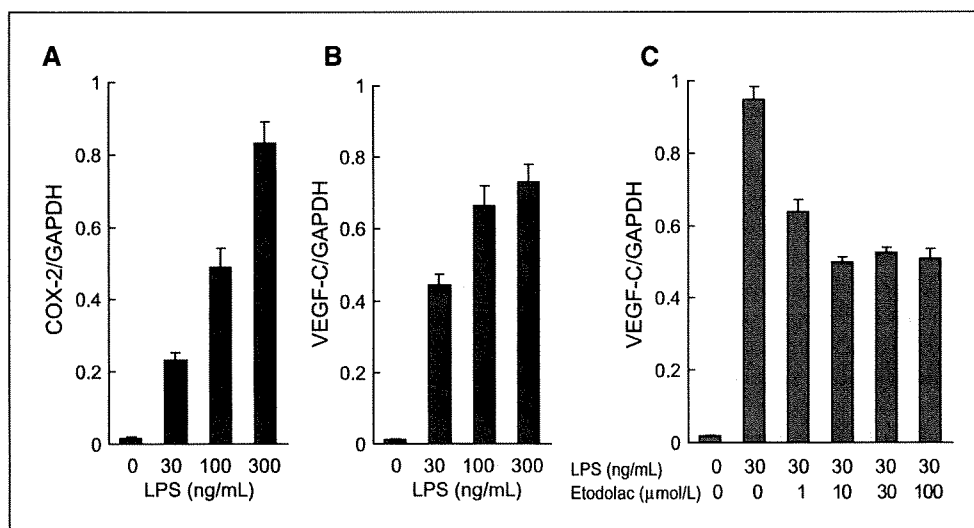
Figure 4. Suppression of expression of VEGF-C by etodolac in macrophages *in vitro*. mRNA levels of COX-2 (*A*) and VEGF-C (*B*) in cultured RAW.264.7, mouse macrophage-like cells, were determined at 24 h after stimulation with LPS. *C*, suppression of VEGF-C expression by treatment with etodolac. *Columns*, mean; *bars*, SE.

treatment with etodolac in a dose-dependent fashion. Ten micro-molars or higher concentrations of etodolac maximally, although not completely, suppressed the expression of VEGF-C mRNA (Fig. 4*C*). We also examined the expression of VEGF-D, but found that it was not significantly affected by etodolac (data not shown).

We further examined the effects of etodolac on cells other than macrophages which are involved in tumor lymphangiogenesis, i.e., lymphatic endothelial cells and cancer cells. We used HDLECs to investigate the effects of etodolac on lymphatic endothelial cells. The mRNA levels of VEGF-R3 in HDLECs were not affected by 10 μmol/L of etodolac (Fig. 5*A*). In contrast, cell growth assay revealed that 3 and 30 μmol/L of etodolac each significantly suppressed the growth of HDLECs, only upon stimulation with LPS, although the inhibitory effect of etodolac was not prominent

(Fig. 5*B*). We also examined the effects of etodolac on the growth of OCUM-2MLN. However, no significant difference in growth of OCUM-2MLN cells was observed at 3 days after addition of 3 or 30 μmol/L etodolac (Fig. 5*C*).

Suppression of lymphangiogenesis by etodolac in a mouse model of chronic inflammation. We used a mouse model of chronic inflammation to determine whether the suppressive effect of etodolac on tumor lymphangiogenesis holds true for inflammatory lymphangiogenesis. In this model, thioglycollate medium was given i.p. as a proinflammatory agent to induce chronic aseptic peritonitis. After repeated i.p. injection (thrice a week for 2 weeks) of thioglycollate medium to immunocompetent BALB/c mice, inflammatory plaques formed on the peritoneal surface of the diaphragm (Fig. 6*A, top*). These plaques were consisted mainly
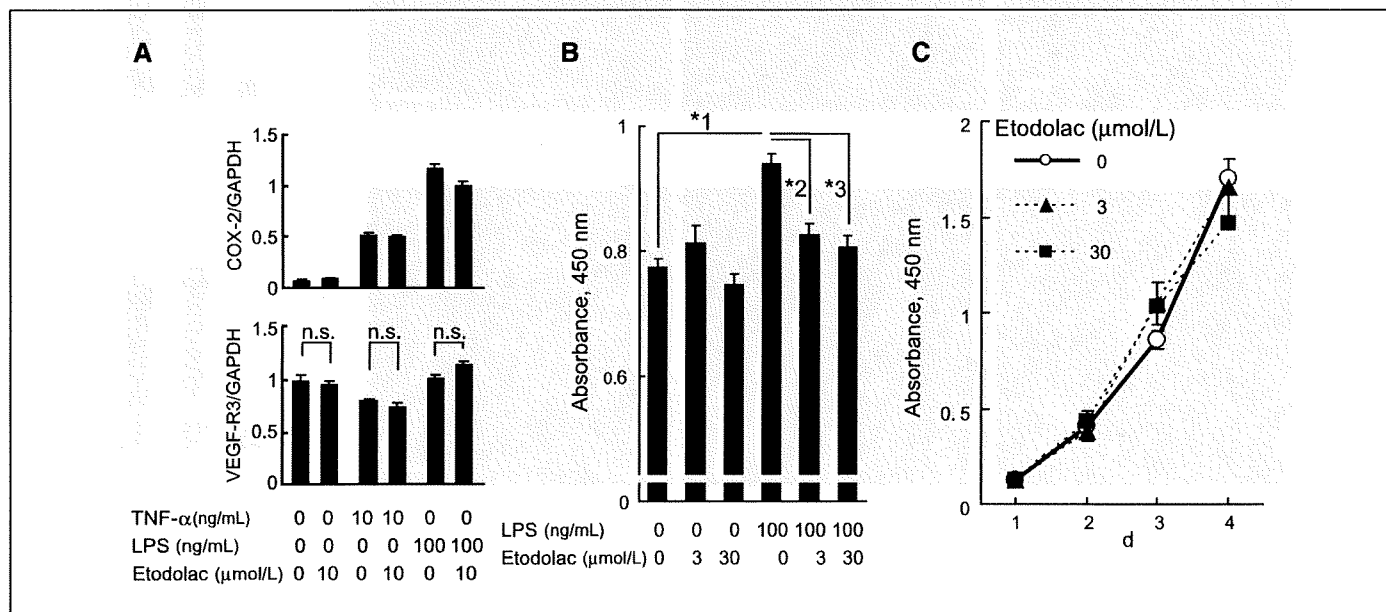

Figure 5. Effects of etodolac on cells other than macrophages. *A*, mRNA levels of VEGF-R3 (*bottom*) in HDLECs treated with 10 μmol/L of etodolac with or without stimulation with 10 ng/mL tumor necrosis factor-α (TNF-α) or 100 ng/mL LPS. *Top*, up-regulation of COX-2 in HDLECs by stimulation with TNF-α or LPS. *Columns*, mean; *bars*, SE. n.s., not significant. *B*, cell growth assay using WST-8 revealed that 3 and 30 μmol/L of etodolac each significantly suppressed the growth of HDLECs upon stimulation with 100 ng/mL LPS; *1, $P < 0.001$; *2, $P < 0.001$; *3, $P < 0.001$; Student's *t* test. *Columns*, mean; *bars*, SE. *C*, cell growth assay with WST-8 revealed that growth of OCUM-2MLN was not affected by etodolac at 3 d after addition of 3 or 30 μmol/L etodolac. *Points*, mean; *bars*, SE.

of mononuclear cells (Fig. 6A, *bottom*). Immunohistochemical analysis revealed that COX-2, VEGF-C, and VEGF-D were highly expressed in these plaques and that many cells positive for VEGF-C and VEGF-D were F4/80-positive macrophages (Fig. 6B).

Using this model, we examined whether etodolac inhibits inflammatory lymphangiogenesis. As shown in Fig. 6C, outgrowths of lymphatic vessels in the plaques were decreased in etodolac-treated mice compared with untreated mice. Quantification of LYVE-1–positive areas in the plaques revealed that induction of lymphangiogenesis was significantly suppressed in etodolac-treated mice compared with control mice (Fig. 6D). These findings indicate that etodolac is able to suppress lymphangiogenesis in tumor tissues, as well as in nontumorous tissue.

Discussion

Many clinical and animal studies have shown that COX-2 induces angiogenesis (34). Meanwhile, there is no direct evidence of a relationship between COX-2 and lymphangiogenesis, although some clinical and animal studies have suggested that level of COX-2 expression in tumor tissue is correlated with lymph node metastasis and/or unfavorable prognosis (24–28, 35). However, none of these studies clearly indicated the status of lymphatic vessels. In the present study, we investigated the effects of COX-2 inhibitor on lymphatic vessels using the lymphatic endothelial cell-specific markers LYVE-1 and Prox1. In the model of lymphatic metastasis, both lymphangiogenesis and angiogenesis were induced around the orthotopic tumors of OCUM-2MLN. We found

Figure 6. Effects of etodolac on lymphangiogenesis in mouse model of chronic aseptic peritonitis. *A, top,* macroscopic appearance of the diaphragm of BALB/c mouse after repeated i.p. injection (thrice a week for 2 wk) of thioglycollate medium. Inflammatory plaques formed on the peritoneal surface of the diaphragm (*arrows*). *Scale bar,* 5 mm. *Bottom,* H&E staining of cross-section of inflammatory plaques on diaphragm. *Scale bar,* 50 μm. *Inset,* enlargement of the boxed area. *B,* immunohistochemical staining of COX-2 (*a and d*), VEGF-C (*b and e*), and VEGF-D (*c and f*) in plaques on diaphragms. Each antibody was displayed in the red channel. *d–f,* double-staining with each antibody and anti-F4/80 (*green*). Nuclear counterstaining was done with TOTO-3 (*blue*). *Scale bars,* 50 μm (*a–c*) and 10 μm (*d–f*). *C,* immunostaining of the inflammatory plaques on diaphragm from control or etodolac-treated mice (*n* = 5 for each group). *Top,* whole-mount staining with the lymphatic vessel marker (anti–LYVE-1, *red*); *middle,* merged images stained also with macrophage marker (anti-CD11b, *green*); *bottom,* cross-sections stained for F4/80 (*green*) and LYVE-1 (*red*). *Scale bar,* 50 μm. *D,* quantification of lymphatic vessels in plaques. *Columns,* mean area densities of LYVE-1–positive pixels per microscopic field; *bars,* SE (10 fields per mouse); ***, *P* < 0.001.
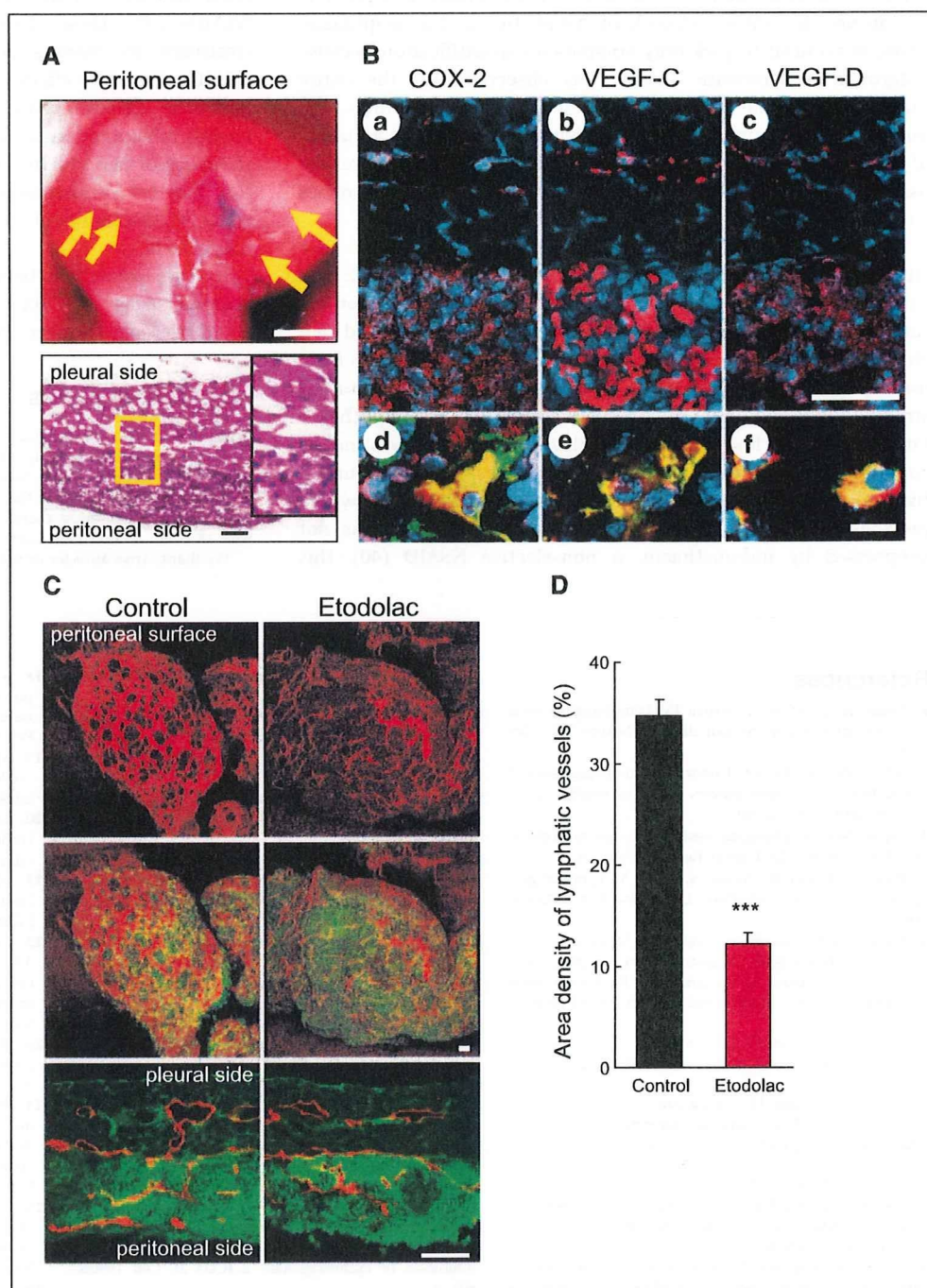
that administration of etodolac suppressed tumor lymphangiogenesis along with tumor angiogenesis. In addition, we evaluated the extent of lymph node metastasis and found that the total weight of metastasized lymph nodes was also decreased by treatment with etodolac. These findings indicated that COX-2 promotes tumor lymphangiogenesis and consequent lymph node metastasis, in addition to tumor angiogenesis as previously reported.

The reproducibility of assignment of highly vascularized areas, i.e., hotspots in tumor tissue sections, is a critical variable in the analysis of lymphangiogenesis (36). Finding relevant hotspots requires training and experience (37). To deal with this potential problem, we established here a new model of tumor lymphangiogenesis in the diaphragm. Since lymphatic vessels in the diaphragm can be immunostained in whole-mount preparations, it is possible to capture the entire network of lymphatics in the diaphragm. There is no need to pick only hotspots for quantification because outgrowth of lymphatic vessels was observed over the entire diaphragm in the model of carcinomatous peritonitis. We quantified the number of sprouts of lymphatic vessels as a marker of lymphangiogenesis, as suggested by Baluk et al. (11). The results using this model confirmed the finding that etodolac suppresses lymphangiogenesis.

Recent studies have shown that inflammatory cells have stimulatory effects on tumor progression (38). In particular, tumor-associated macrophages have been suggested to promote tumor lymphangiogenesis (10, 39). We therefore hypothesized that etodolac suppresses the secretion of lymphangiogenic factors from macrophages. Our finding that some macrophages in tumor stroma expressed COX-2 strongly supports this hypothesis. Furthermore, we found that mRNA levels of VEGF-C was indeed suppressed by etodolac in RAW264.7 cells, as well as in tumor tissues *in vivo*. Although these findings are not in agreement with a previous report that VEGF-C expression in fibroblasts was not suppressed by indomethacin, a nonselective NSAID (40), this discrepancy may be due to the difference in cell types examined or the COX-2 selectivity of drugs used.

Lymphangiogenesis is also induced in chronic inflammatory lesions (41). Macrophages have recently been shown to be recruited into inflammatory lesions to secrete VEGF-C and induce lymphangiogenesis (11, 12). In the present study, using a model of chronic aseptic peritonitis, we observed that macrophages densely accumulated in inflammatory plaques, wherein lymphangiogenic growth factors are expressed. These findings suggest that COX-2 can enhance lymphangiogenesis in the absence of cancer cells.

We have shown that decrease of lymph node metastasis can be achieved by COX-2 inhibitor, possibly via inhibition of macrophage-mediated lymphangiogenesis. Despite recent studies reporting cardiovascular complications from long-term administration of NSAIDs (42), these drugs may still be applicable to cancer treatment by limiting population and administrating periods: NSAIDs should be effective for preventing potential metastases in patients with advanced cancers in presurgical period or in those having inflammation aroused by surgical manipulation in early postsurgical periods. In the latter case, surgery-related inflammation may be accompanied by lymphangiogenesis, which can be a cause of dissemination or metastasis of unexpectedly remained cancer cells.

In conclusion, we believe that our findings may provide a potential usage of COX-2 inhibitors in cancer treatment, which could overcome known obstacles in using these drugs.

References

1. Alitalo K, Tammela T, Petrova TV. Lymphangiogenesis in development and human disease. Nature 2005;438: 946–53.
2. Achen MG, Stacker SA. Tumor lymphangiogenesis and metastatic spread-new players begin to emerge. Int J Cancer 2006;119:1755–60.
3. Pepper MS. Lymphangiogenesis and tumor metastasis: myth or reality? Clin Cancer Res 2001;7:462–8.
4. Pepper MS, Tille JC, Nisato R, Skobe M. Lymphangiogenesis and tumor metastasis. Cell Tissue Res 2003;314: 167–77.
5. Nakamura Y, Yasuoka H, Tsujimoto M, et al. Importance of lymph vessels in gastric cancer: a prognostic indicator in general and a predictor for lymph node metastasis in early stage cancer. J Clin Pathol 2006;59: 77–82.
6. Achen MG, McColl BK, Stacker SA. Focus on lymphangiogenesis in tumor metastasis. Cancer Cell 2005;7:121–7.
7. Shimizu K, Kubo H, Yamaguchi K, et al. Suppression of VEGFR-3 signaling inhibits lymph node metastasis in gastric cancer. Cancer Sci 2004;95: 328–33.
8. Yonemura Y, Endo Y, Fujita H, et al. Role of vascular endothelial growth factor C expression in the development of lymph node metastasis in gastric cancer. Clin Cancer Res 1999;5:1823–9.
9. Kitadai Y, Kodama M, Cho S, et al. Quantitative analysis of lymphangiogenic markers for predicting metastasis of human gastric carcinoma to lymph nodes. Int J Cancer 2005;115:388–92.
10. Schoppmann SF, Birner P, Stockl J, et al. Tumor-associated macrophages express lymphatic endothelial growth factors and are related to peritumoral lymphangiogenesis. Am J Pathol 2002;161:947–56.
11. Baluk P, Tammela T, Ator E, et al. Pathogenesis of persistent lymphatic vessel hyperplasia in chronic airway inflammation. J Clin Invest 2005;115:247–57.
12. Cursiefen C, Chen L, Borges LP, et al. VEGF-A stimulates lymphangiogenesis and hemangiogenesis in inflammatory neovascularization via macrophage recruitment. J Clin Invest 2004;113:1040–50.
13. Thun MJ, Henley SJ, Patrono C. Nonsteroidal anti-inflammatory drugs as anticancer agents: mechanistic, pharmacologic, and clinical issues. J Natl Cancer Inst 2002;94:252–66.
14. Dannenberg AJ, Altorki NK, Boyle JO, et al. Cyclooxygenase 2: a pharmacological target for the prevention of cancer. Lancet Oncol 2001;2:544–51.
15. Ristimaki A, Honkanen N, Jankala H, Sipponen P, Harkonen M. Expression of cyclooxygenase-2 in human gastric carcinoma. Cancer Res 1997;57:1276–80.
16. Saukkonen K, Nieminen O, van Rees B, et al. Expression of cyclooxygenase-2 in dysplasia of the stomach and in intestinal-type gastric adenocarcinoma. Clin Cancer Res 2001;7:1923–31.
17. Oshima M, Dinchuk JE, Kargman SL, et al. Suppression of intestinal polyposis in Apc$^{\Delta716}$ knockout mice by inhibition of cyclooxygenase 2 (COX-2). Cell 1996;87: 803–9.
18. Kawamori T, Rao CV, Seibert K, Reddy BS. Chemopreventive activity of celecoxib, a specific cyclooxygenase-2 inhibitor, against colon carcinogenesis. Cancer Res 1998;58:409–12.
19. Wang D, Mann JR, DuBois RN. The role of prostaglandins and other eicosanoids in the gastrointestinal tract. Gastroenterology 2005;128:1445–61.
20. Tsujii M, Kawano S, Tsuji S, Sawaoka H, Hori M, DuBois RN. Cyclooxygenase regulates angiogenesis induced by colon cancer cells. Cell 1998;93:705–16.
21. Williams CS, Tsujii M, Reese J, Dey SK, DuBois RN. Host cyclooxygenase-2 modulates carcinoma growth. J Clin Invest 2000;105:1589–94.
22. Leahy KM, Ornberg RL, Wang Y, Zweifel BS, Koki AT, Masferrer JL. Cyclooxygenase-2 inhibition by celecoxib reduces proliferation and induces apoptosis in angiogenic endothelial cells *in vivo*. Cancer Res 2002; 62:625–31.
23. Masferrer JL, Leahy KM, Koki AT, et al. Antiangiogenic and antitumor activities of cyclooxygenase-2 inhibitors. Cancer Res 2000;60:1306–11.
24. Su JL, Shih JY, Yen ML, et al. Cyclooxygenase-2 induces EP1- and HER-2/Neu-dependent vascular endothelial growth factor-C up-regulation: a novel mechanism of lymphangiogenesis in lung adenocarcinoma. Cancer Res 2004;64:554–64.
25. Timoshenko AV, Chakraborty C, Wagner GF, Lala PK. COX-2-mediated stimulation of the lymphangiogenic factor VEGF-C in human breast cancer. Br J Cancer 2006;94:1154–63.
26. Siironen P, Ristimaki A, Narko K, et al. VEGF-C and

COX-2 expression in papillary thyroid cancer. Endocr Relat Cancer 2006;13:465–73.

27. Soumaoro LT, Uetake H, Takagi Y, et al. Coexpression of VEGF-C and Cox-2 in human colorectal cancer and its association with lymph node metastasis. Dis Colon Rectum 2006;49:392–8.

28. Zhang J, Ji J, Yuan F, et al. Cyclooxygenase-2 expression is associated with VEGF-C and lymph node metastases in gastric cancer patients. Biomed Pharmacother 2005;59 [Suppl]:S285–8.

29. Glaser K, Sung ML, O'Neill K, et al. Etodolac selectively inhibits human prostaglandin G/H synthase 2 (PGHS-2) versus human PGHS-1. Eur J Pharmacol 1995;281:107–11.

30. Warner TD, Giuliano F, Vojnovic I, Bukasa A, Mitchell JA, Vane JR. Nonsteroid drug selectivities for cyclo-oxygenase-1 rather than cyclo-oxygenase-2 are associated with human gastrointestinal toxicity: a full *in vitro* analysis. Proc Natl Acad Sci U S A 1999;96:7563–8.

31. Fujihara T, Sawada T, Hirakawa K, et al. Establishment of lymph node metastatic model for human gastric cancer in nude mice and analysis of factors associated with metastasis. Clin Exp Metastasis 1998;16: 389–98.

32. Shibuya K, Shirakawa J, Kameyama T, et al. CD226 (DNAM-1) is involved in lymphocyte function-associated antigen 1 costimulatory signal for naive T cell differentiation and proliferation. J Exp Med 2003;198: 1829–39.

33. Abu-Hijleh MF, Habbal OA, Moqattash ST. The role of the diaphragm in lymphatic absorption from the peritoneal cavity. J Anat 1995;186:453–67.

34. Iniguez MA, Rodriguez A, Volpert OV, Fresno M, Redondo JM. Cyclooxygenase-2: a therapeutic target in angiogenesis. Trends Mol Med 2003;9:73–8.

35. Tendo M, Yashiro M, Nakazawa K, et al. Inhibitory effect of a selective cyclooxygenase inhibitor on the invasion-stimulating activity of orthotopic fibroblasts for scirrhous gastric cancer cells. Cancer Sci 2005;96: 451–5.

36. Van der Auwera I, Cao Y, Tille JC, et al. First international consensus on the methodology of lymphangiogenesis quantification in solid human tumours. Br J Cancer 2006;95:1611–25.

37. Vermeulen PB, Gasparini G, Fox SB, et al. Second international consensus on the methodology and criteria of evaluation of angiogenesis quantification in solid human tumours. Eur J Cancer 2002; 38:1564–79.

38. Coussens LM, Werb Z. Inflammation and cancer. Nature 2002;420:860–7.

39. Dadras SS, Paul T, Bertoncini J, et al. Tumor lymphangiogenesis: a novel prognostic indicator for cutaneous melanoma metastasis and survival. Am J Pathol 2003;162:1951–60.

40. Ristimaki A, Narko K, Enholm B, Joukov V, Alitalo K. Proinflammatory cytokines regulate expression of the lymphatic endothelial mitogen vascular endothelial growth factor-C. J Biol Chem 1998;273:8413–8.

41. Pullinger BD, Florey HW. Proliferation of lymphatics in inflammation. J Pathol Bact 1937;45:157–70.

42. Antman EM, Bennett JS, Daugherty A, Furberg C, Roberts H, Taubert KA. Use of nonsteroidal antiinflammatory drugs: an update for clinicians: a scientific statement from the American Heart Association. Circulation 2007;115:1634–42.

ELSEVIER

Optimization of (1,2-diamino-cyclohexane)platinum(II)-loaded polymeric micelles directed to improved tumor targeting and enhanced antitumor activity

Horacio Cabral [a], Nobuhiro Nishiyama [b], Kazunori Kataoka [a,b,c,*]

[a] Department of Materials Engineering, Graduate School of Engineering, The University of Tokyo, 7-3-1 Hongo, Bunkyo-ku, Tokyo 113-8656, Japan
[b] Center for Disease Biology and Integrative Medicine, Graduate School of Medicine, The University of Tokyo, 7-3-1 Hongo, Bunkyo-ku, Tokyo 113-0033, Japan
[c] Center for NanoBio Integration, The University of Tokyo, 7-3-1 Hongo, Bunkyo-ku, Tokyo, 113-8656, Japan

Abstract

Polymeric micelles are promising nanocarriers, which might enhance the efficacy of antitumor drugs. Herein, polymeric micelles incorporating dichloro(1,2-diamino-cyclohexane)platinum(II) (DACHPt), the oxaliplatin parent complex, were prepared through the polymer-metal complex formation of DACHPt with poly(ethylene glycol)-b-poly(glutamic acid) [PEG-b-P(Glu)] block copolymer having different lengths of the poly (glutamic acid) block [p(Glu): 20, 40, and 70 U]. The resulting micelles were studied with the aim of optimizing the system's biological performance. DACHPt-loaded micelles (DACHPt/m) were approximately 40 nm in diameter and had a narrow size distribution. *In vivo* biodistribution and antitumor activity experiments (CDF$_1$ mice bearing the murine colon adenocarcinoma C-26 inoculated subcutaneously) showed 20-fold greater accumulation of DACHPt/m at the tumor site than free oxaliplatin to achieve substantially higher antitumor efficacy. Moreover, the micelles prepared from PEG-b-P(Glu) with 20 U of P(Glu) exhibited the lowest non-specific accumulation in the liver and spleen to critically reduce non-specific accumulation, resulting in higher specificity to solid tumors. The antitumor effect of DACHPt/m was also evaluated on multiple metastases generated from intraperitoneally injected bioluminescent HeLa (HeLa-Luc) cells. The *in vivo* bioluminescent data indicated that DACHPt/m decreased the signal 10-to 50-fold compared to the control indicating a very strong antitumor activity. These results suggest that DACHPt/m could be an outstanding drug delivery system for oxaliplatin in the treatment of solid tumors.
© 2007 Elsevier B.V. All rights reserved.

Keywords: Polymeric micelles; DACHPt; Oxaliplatin; Biodistribution; Antitumor activity

1. Introduction

Oxaliplatin, oxalato(trans-*l*-1,2-diaminocyclohexane)platinum(II), is a third-generation platinum drug approved by the United States Food and Drug Administration in 2004 for the first-line treatment of advanced colorectal cancer in combination with 5-fluorouracil/folinic acid (5-FU/LV) [1]. The incorporation of oxaliplatin into the colorectal cancer program represents a major improvement in the treatment of the disease.

The synergistic effects between oxaliplatin and 5-FU/LV significantly increased the response rates, improved the time-sensitive response parameters, and contributed to the removal of heretofore unresectable hepatic metastases, thereby changing the natural history of the malignancy. Nevertheless, oxaliplatin distributes rapidly to the whole body and, even though it shows better tolerability relative to other platinum drugs, cumulative peripheral distal neurotoxicity and acute dysesthesias restrain the range of working doses [2,3]. Consequently, enormous effort has been dedicated to develop drug delivery systems that increase the blood residence time of oxaliplatin and other platinum drugs, and target those drugs to solid tumors by taking advantage of the enhanced permeability and retention (EPR) effect [4]. Liposomes and macromolecular carriers (water soluble polymer–drug conjugates) have been the first attempts

* Corresponding author. Department of Materials Engineering, Graduate School of Engineering, The University of Tokyo, 7-3-1 Hongo, Bunkyo-ku, Tokyo 113-8656, Japan. Tel.: +81 3 5841 7138; fax: +81 3 5841 7139.
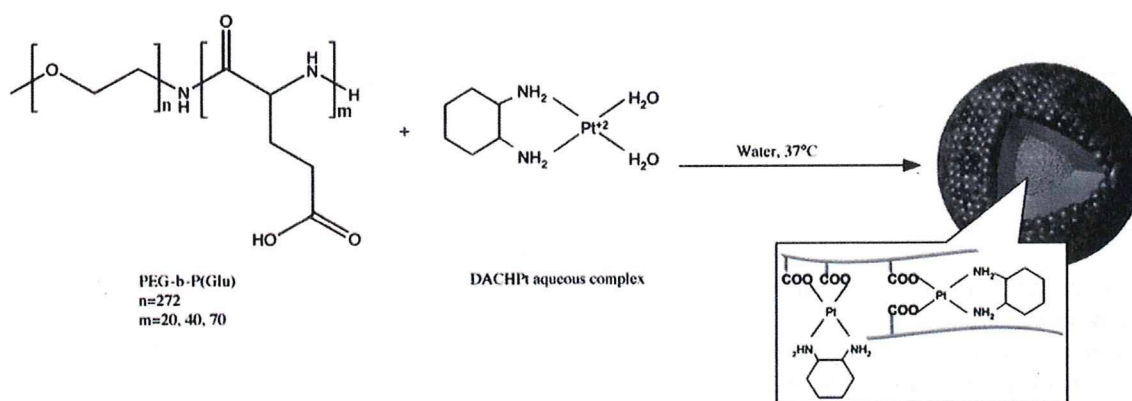*E-mail address:* kataoka@bmw.t.u-tokyo.ac.jp (K. Kataoka).

Fig. 1. Formation of DACHPt-loaded micelle (DACHPt/m).

to be considered [5–11]. However, successful formulations have not been developed yet due to unfavorable properties of platinum drugs. For example, the low water solubility of platinum drugs limits their loading efficacy into liposomal formulations (only 1 to 7% of drug loading). Moreover, liposomes incorporating the drug in the lipid bilayer showed rapid leakage of the drugs during storage and in the bloodstream [6]. In the case of macromolecular-drug formulations at high substitution ratios, they show reduced solubility due to the enlarged cohesive forces and to the cross-linking formation between polymer chains [8].

A novel approach to the design of nanocarriers for platinum drugs has been utilizing polymeric micelles [12–15]. Polymeric micelles present unique advantages over other types of drug-carrier systems: (i) prolonged blood circulation due to the efficient stealthy behavior of the dense shell of poly(ethylene glycol) (PEG), which hinders the adsorption of plasma proteins on the surface of the nanostructure and avoids recognition by the reticuloendothelial system (RES); (ii) easiness in encapsulating different compounds by modulating the micelle-forming block copolymers; (iii) reduced cumulative toxicity because of the micellar self-dissociation into unimers with molecular weight lower than that of the threshold of glomerular excretion; (iv) simplicity in size control by changing the chemical composition of block copolymers; (v) deeper tumor penetration due to the sub-100 nm size; (vi) facile management of the drug release in a controlled and environment-sensitive manner by modification of the drug-polymer system; and (vii) improved targeting capability by conjugating pilot molecules on the surface of micelles.

The first generation of platinum-drug-loaded micelles was prepared by the metal-complex formation between cis-dichlorodiammineplatinum(II) (cisplatin, CDDP) and poly(ethylene glycol)-b-poly(amino acid) block copolymers [16–21]. The exceptional physicochemical and biological properties of the CDDP-loaded micelle indicate them as an outstanding delivery system for CDDP complexes and a phase I clinical trial is being performed in United Kingdom (NC-6004, Nanocarrier, Japan). More recently, new platinum-drug-loaded polymeric micelles incorporating the oxaliplatin active complex were prepared by the complexation of dichloro(1,2-diaminocyclohexane)platinum(II) (DACHPt) with PEG-b-P(Glu) [22]. Previous studies

demonstrated that the DACHPt-loaded micelle (DACHPt/m) might maintain its micellar structure for approximately 10 days in 10 mM PBS plus 150 mM NaCl, considerably longer than the stability of the CDDP-loaded micelles (ca 50 h) under the same conditions, while the drug was released from the micelle core in a sustained manner. Moreover, DACHPt/m showed remarkably prolonged blood circulation and more than 20-fold greater accumulation in tumor tissue compared to free oxaliplatin. According to these results, DACHPt/m seems to be an exceptionally promising carrier for the active complexes of oxaliplatin.

Herein, the in vitro and in vivo biological properties of DACHPt/m prepared with poly(ethylene glycol)-b-poly(glutamic acid) [PEG-b-P(Glu)] were studied with the aim of optimizing the biological performance of the micelle. Thus, PEG-b-P(Glu) having different P(Glu) block lengths (20, 40, and 70 U) were synthesized and used for the micelle preparation. DACHPt/m was phisicochemically characterized to determine the size, size distribution, zeta-potential, drug loading, and weight fraction of block copolymer. The in vivo behavior of DACHPt/m was assessed by the biodistribution and antitumor activity experiments using CDF_1 mice bearing the murine colon adenocarcinoma 26 (C-26). Although oxaliplatin had shown low efficacy against this tumor model [23], we found that DACHPt/m considerably increased the antitumor activity of the drug, probably by maintaining high drug levels within the tumor for a prolonged period. Furthermore, since chemotherapy is used in patients with metastatic disease and all the established therapies reveal poor efficiency at the late stage of the disease [24], new therapeutic strategies are urgently needed. Moreover, given that the very low prognosis of late-stage cervical carcinoma [25] (5 years after treatment 15% or fewer of women with stage IV cancer survive) is mainly due to metastasis to the abdomen or the lungs, the antitumor activity of DACHPt/m was evaluated against a bioluminescent intraperitoneal metastatic tumor model of cervical cancer.

2. Experimental

2.1. Materials

γ-benzyl L-glutamate was purchased from Sigma Chemical (St. Louis, MO). Bis(trichloromethyl)carbonate (triphosgene) was purchased from Tokyo Kasei Kogyo (Tokyo, Japan). N,N-

Table 1
DACHPt-loaded micelles (DACHPt/m) size, zeta-potential and drug loading

Micelle formulation	Size(nm)	Zeta-potential(mV)	Drug loading, [DACHPt]/[Glu]
DACHPt/m 12–20	37	−3	0.317
DACHPt/m 12–40	40	−4	0.323
DACHPt/m 12–70	41	−4	0.288

dimethylformamide (DMF) and 3-(4,5-dimethylthiazol-2-yl)-2,5-diphenyltetrazolium bromide (MTT) were obtained from Wako Pure Chemical (Osaka, Japan). Dichloro(1,2-diammino-cyclohexane)platinum(II) (DACHPt) and $AgNO_3$ were purchased from Aldrich Chemical (Milwaukee, WI). α-methoxy-ω-aminopoly(ethylene glycol) (CH_3O–PEG–NH_2; Mw= 12,000) was purchased from Nippon Oil and Fats (Tokyo, Japan).

2.2. Cell lines and animals

Murine colon adenocarcinoma 26 (C-26) cells were kindly supplied by the National Cancer Center (Tokyo, Japan). C-26 cells were maintained in RPMI 1640 medium (Sigma Chemical) containing 10% fetal bovine serum in a humidified atmosphere containing 5% CO_2 at 37 °C. Bioluminescent HeLa (HeLa-Luc) cells were purchased from Xenogen (Alameda, CA). Luciferase stable-HeLa-Luc cells were maintained in Dulbecco's Modified Eagle Medium (Sigma Chemical Co., Inc.) containing 10% fetal

Table 2
Accumulation ratios and area under the curve (AUC) ratios between tumor and normal organs at 48 h after administration of DACHPt-loaded micelles (DACHPt/m)[a] prepared with PEG-b-P(Glu) 12–40 and free oxaliplatin

Drug	Accumulation ratio				AUC ratio[b]		
	Tumor/ liver	Tumor/ spleen	Tumor/ kidney	Tumor/ liver	Tumor/ spleen	Tumor/ kidney
DACHPt/m 12–40	1.25	1.26	3.9	1.25	1.53	3.12
Oxaliplatin	0.9	0.18	0.42	1.1	0.32	0.9

[a] Dose: 0.1 mg per mouse on Pt basis.
[b] AUC calculated by trapezoidal rule up to 48 h.

bovine serum in a humidified atmosphere containing 5% CO_2 at 37 °C for no more than two weeks to assure luciferase luminescence stability.

Severe Combined Immunodeficiency (SCID) and CDF_1 mice (female; 18–20 g body weight; 6 weeks old) were purchased from Charles River Japan (Kanagawa, Japan). All animal experiments were carried out in accordance with the Guide for the Care and Use of Laboratory Animals as stated by the NIH. Sterile procedures were followed to assure that SCID mice were disease-free.

2.3. Preparation of PEG-b-P(Glu)

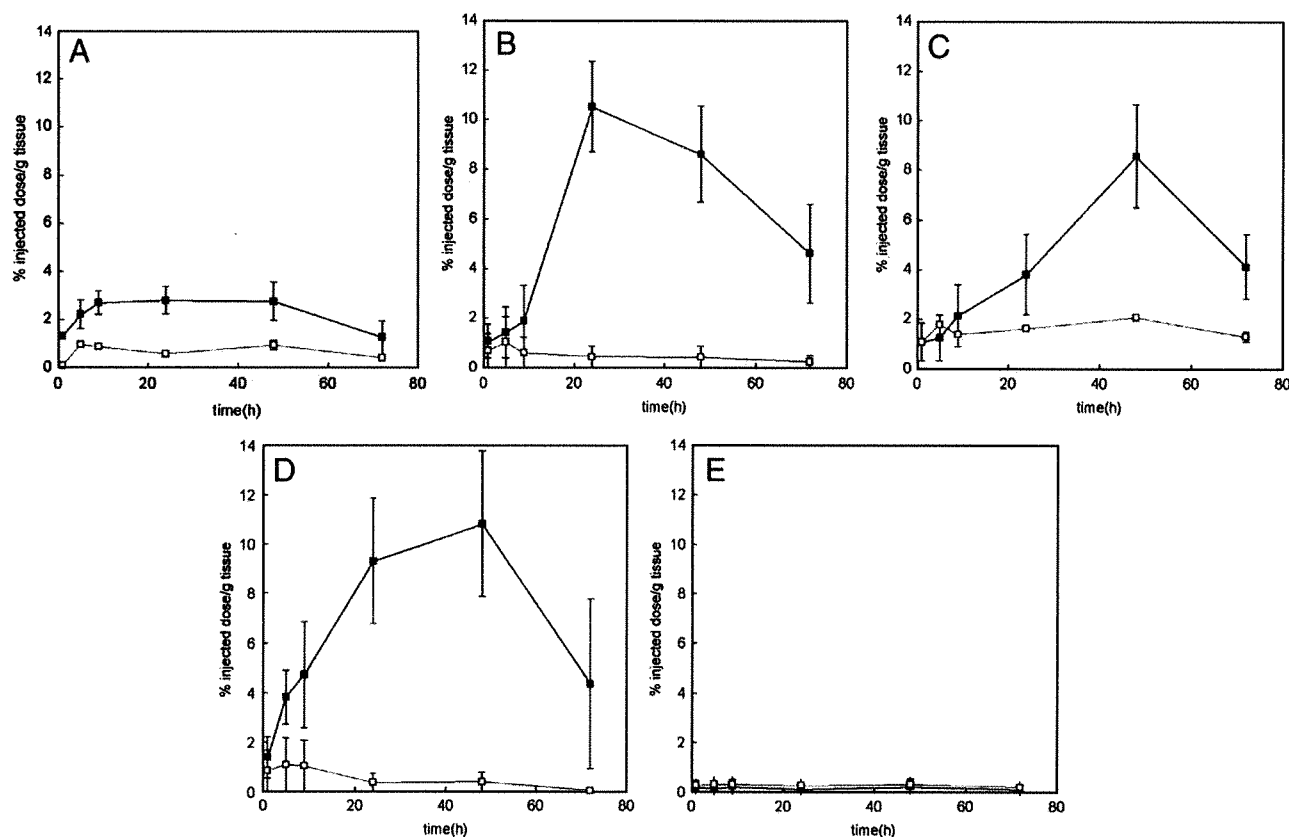PEG-b-P(Glu) block copolymers were synthesized in accordance with the previously described synthetic method

Fig. 2. Biodistribution of oxaliplatin (□) and DACHPt-loaded micelle (DACHPt/m) prepared with PEG-b-P(Glu) 12–40 (■): A. Kidney; B. Liver; C. Spleen; D. Tumor; E. Muscle. Data are expressed as averages±S.D.

[20] with a minor modification. Briefly, the *N*-carboxy anhydride of γ-benzyl L-glutamate was synthesized by the Fuchs–Farthing method using triphosgene. Then, *N*-carboxy anhydride of γ-benzyl L-glutamate was polymerized in DMF, initiated by the primary amino group of $CH_3O–PEG–NH_2$, to obtain PEG-*b*-poly(γ-benzyl L-glutamate) (PEG-*b*-PBLG) block copolymer with different PBLG block lengths (20, 40, and 70 U). The molecular weight distribution of PEG-*b*-PBLG was determined by gel permeation chromatography [column: TSK-gel G3000$_{HHR}$, G4000$_{HHR}$ (Tosoh, Yamaguchi, Japan); eluent: DMF containing 10 mM LiCl; flow rate: 0.8 ml/min; detector: refractive index (RI); temperature: 25 °C]. The polymerization degree of PBLG was verified by comparing the proton ratios of methylene units in PEG ($–OCH_2CH_2–$: $δ=3.7$ ppm) and phenyl groups of PBLG ($–CH_2C_6H_5$: $δ=7.3$ ppm) in ^{1}H-NMR measurement [JEOL EX270 (JEOL, Tokyo, Japan); solvent: DMSO-d$_6$; temperature: 80 °C]. PEG-*b*-PBLG was deprotected by mixing with 0.5 N NaOH at room temperature to obtain PEG-*b*-P(Glu). Complete deprotection was confirmed by ^{1}H-NMR measurement (solvent: D$_2$O; temperature: 25 °C). The compositions of PEG-*b*-P(Glu) are abbreviated as PEG-*b*-P(Glu) 12–20, PEG-*b*-P(Glu) 12–40 and PEG-*b*-P(Glu) 12–70 for the different P(Glu) block lengths (20, 40, and 70 U, respectively).

2.4. Preparation of DACHPt-loaded micelles (DACHPt/m)

DACHPt/m were prepared according to a previously described method [22]. Briefly, DACHPt (5 mM) was suspended in distilled water and mixed with silver nitrate ($[AgNO_3]$/ $[DACHPt]=1$) to form an aqueous complex. The solution was kept in the dark at 25 °C for 24 h. AgCl precipitates found after the reaction were eliminated by centrifugation. Afterward, the supernatant was purified by passage through a 0.22 μm filter. Then, PEG-*b*-P(Glu) 12–20, 12–40, or 12–70 ([Glu]=5 mmol/ liter) was added to DACHPt aqueous complex solution ($[DACHPt]/[Glu]=1.0$) and reacted for 120 h to prepare DACHPt/m. The prepared micelles were purified by ultrafiltration [molecular weight cutoff size (MWCO): 100,000]. The size distribution of DACHPt/m was evaluated by the dynamic light scattering (DLS) measurement at 25 °C using a Photal DLS-7000 dynamic laser scattering spectrometer (Otsuka Electronics, Osaka, Japan). The zeta-potential of DACHPt/m was determined using a Zetasizer Nano ZS90 (Malvern Instruments, Worcestershire, United Kingdom). The Pt content of the micelles was determined by an ion coupled plasma-mass spectrometer (4500 ICP-MS; Hewlett Packard, Palo Alto, CA).

2.5. Biodistribution

In order to analyze the fate of oxaliplatin and DACHPt/m *in vivo*, CDF$_1$ mice (female, $n=6$) were injected subcutaneously with C-26 cells ($1×10^6$ cells/ml). Fourteen days later, oxaliplatin or DACHPt/m prepared with PEG-*b*-P(Glu) 12–40 were intravenously injected by the tail vein at a dose of 100 μg/ mouse on a platinum basis. Mice were sacrificed after defined time periods (1, 4, 8, 24, 48, and 72 h).

To assess the effect of formulation on the tissue distribution, CDF$_1$ mice (female, $n=6$) bearing s.c. C-26 tumors were intravenously administered oxaliplatin or DACHPt/m prepared with PEG-*b*-P(Glu) with different P(Glu) lengths (20, 40, and
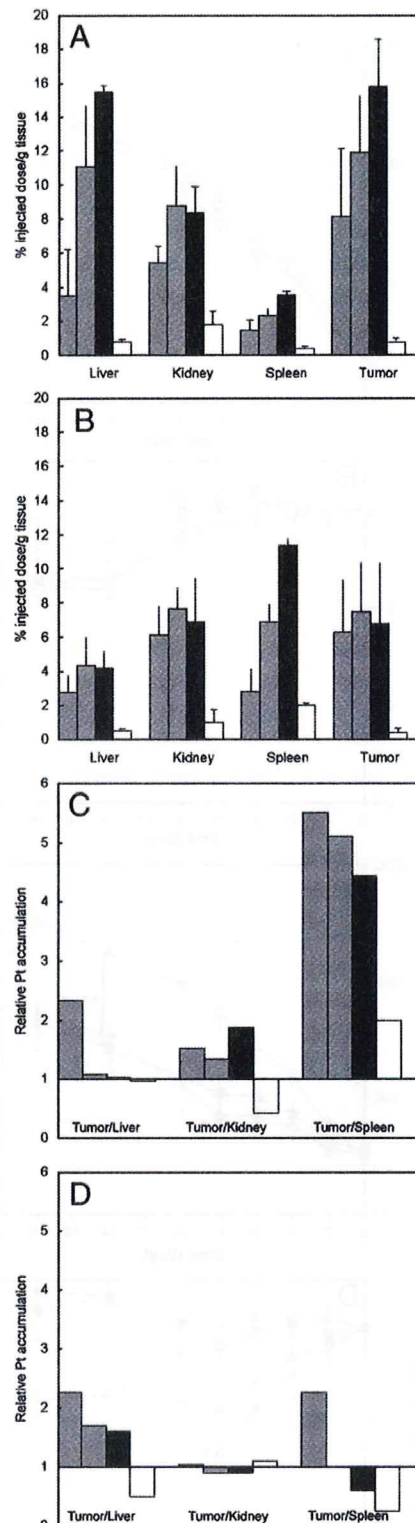

Fig. 3. Biodistribution of DACHPt-loaded micelle (DACHPt/m) prepared with PEG-*b*-P(Glu) 12–20(▨), PEG-*b*-P(Glu) 12–40(▧), PEG-*b*-P(Glu) 12–70(■) and oxaliplatin (□): A. 24 h; B.48 h; C. 24 h tumor/organ ratio; D. 48 h tumor/ organ ratio. Data are expressed as averages±S.D.

70 U) at 100 µg/mouse on a platinum basis. Mice were sacrificed at 24 and 48 h post-incubation.

Tumor, liver, kidney, spleen, and muscle were collected. Blood was collected from the inferior vena cava, heparinized

and centrifuged to obtain the plasma. Tissue samples were washed in ice-cold saline and weighed after removing excess fluid. All samples were dissolved in HNO_3 and evaporated to dryness. The Pt concentration was measured by ICP-MS after the samples were redissolved in 5 N HCl. The area under the curve (AUC) was calculated by the trapezoidal rule.

2.6. Antitumor activity assay

CDF_1 mice (female, $n=6$) were inoculated subcutaneously with C-26 cells (1×10^6 cells/ml). Tumors were allowed to grow for 1 week (the size of tumor at this point was approximately 30 mm^3 or 100 mm^3). Subsequently, mice were treated i.v. 4 times at 2-day intervals at doses of 2, 4, 6 and 10 mg/kg of oxaliplatin or 2, 4 and 6 mg/kg (on a platinum base) of DACHPt/m prepared with PEG-b-P(Glu) 12–20 or PEG-b-P (Glu) 12–40. The antitumor activity was evaluated in terms of tumor size (V), as estimated by the following equation:

$$V = a \times b^2/2$$

where a and b are the major and minor axes of the tumor measured by a caliper, respectively. The body weight was measured simultaneously and was taken as a parameter of systemic toxicity. The statistical analysis of animal data was carried out by the unpaired t-test.

2.7. Antitumor activity in a bioluminescent intraperitoneal metastasis model

SCID mice (female, $n=5$) were inoculated intraperitoneally with Hela-Luc cells (5×10^5 cells/ml). Tumors were allowed to grow for 3 days. Subsequently, mice were treated i.v. 3 times at 2-day intervals at doses of 4 and 6 mg/kg (on a platinum base) of oxaliplatin or DACHPt/m prepared with PEG-b-P(Glu) 12–20. In vivo bioluminescent imaging (BLI) was performed with an IVIS Imaging System (Xenogen) comprised of a highly sensitive, cooled CCD camera mounted in a light-tight specimen box. Images and measurements of bioluminescent signals were acquired and analyzed using Living Image software (Xenogen). Ten minutes prior to in vivo imaging, animals received the substrate D-luciferin (Biosynth) at 150 mg/kg in PBS by intraperitoneal injection and were anesthetized using 1–3% isoflurane (Abbott Laboratories, North Chicago, IL). Animals were placed onto a warmed stage inside the camera box and received continuous exposure to 1–2% isoflurane to sustain sedation during imaging. Imaging times ranged from 10 to 60 s, depending on the bioluminescence of the metastatic lesions. Five mice were imaged at a time. Tumor growth was monitored
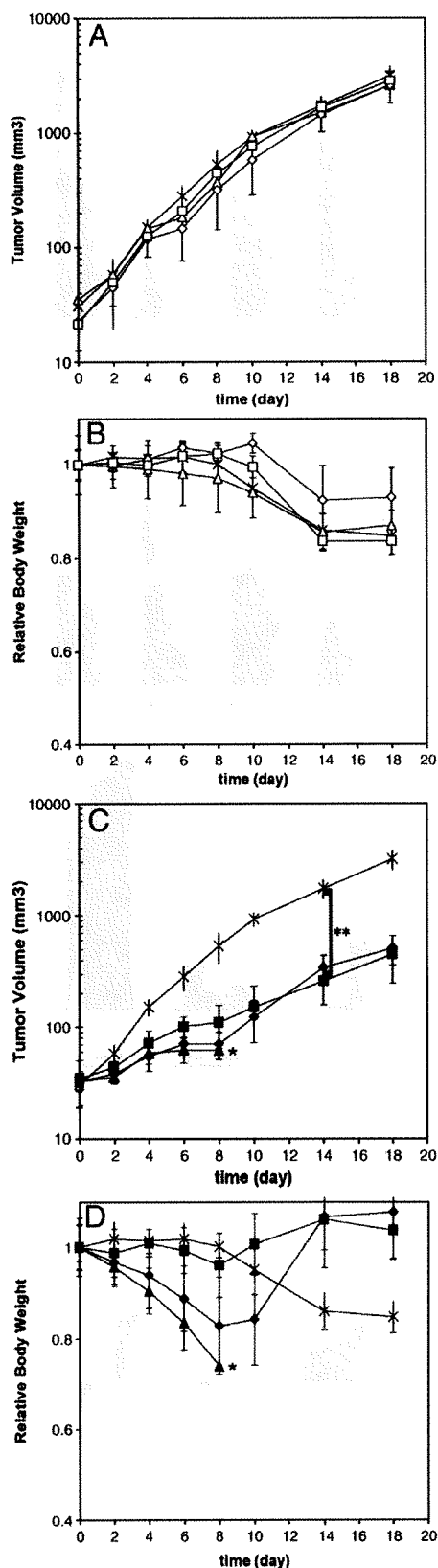

Fig. 4. Antitumor activity of DACHPt-loaded micelle (DACHPt/m) prepared with PEG-b-P(Glu) 12–40 against s.c. C-26 tumor model ($n=5$). Saline(×); oxaliplatin at 6 mg/kg(△); 4 mg/kg(◇); 2 mg/kg(□). DACHPt-loaded micelle (DACHPt/m) 12–40 at 6 mg/kg(▲); 4 mg/kg(◆); 2 mg/kg(■). A. Tumor volume (mm^3) for oxaliplatin treatment; B. Relative body weight of mice for oxaliplatin treatment; C. Tumor volume (mm^3) for DACHPt/m treatment; D. Relative body weight of mice for DACHPt/m treatment. Data are expressed as averages ± S.D. *Toxic death. **$p<0.001$.

by BLI every second day for 18 days. The light emitted from the bioluminescent tumors was detected *in vivo* by the IVIS Imaging System, was digitized and electronically displayed as a pseudocolor overlay onto a gray scale animal image. Regions of interest (ROI) from displayed images were drawn around the tumor sites and quantified as photons/second using the Living Image software. The statistical analysis of animal data was carried out by the unpaired *t*-test.

3. Results

3.1. Micelle characterization

The metal-polymer complex formation between DACHPt and the carboxylic group of the p(Glu) in the PEG-*b*-P(Glu) led to the formation of narrowly distributed micellar assemblies (Fig. 1) with average diameters of approximately 40 nm (Table 1). The increase in the length of the p(Glu) block slightly enlarged the diameter of DACHPt/m (Table 1). The drug content in the micelles was determined to be remarkably high in all the micelle formulations (Table 1). The [DACHPt]/[Glu] molar ratios in DACHPt/m were found to be similar for all the formulations.

3.2. Biodistribution

3.2.1. Biodistribution of free oxaliplatin and DACHPt/m prepared with PEG-b-P(Glu) 12–40

The biodistribution study was performed on CDF_1 mice ($n=6$) bearing s.c. C-26 tumors. Oxaliplatin or DACHPt/m prepared with PEG-*b*-P(Glu) 12–40 were i.v. injected. In previous studies, DACHPt/m prepared with PEG-*b*-P(Glu) 12–40 have shown remarkably prolonged blood circulation, whereas free oxaliplatin was promptly removed from circulation. The Pt in plasma was determined to be 15% of the injected dose at 24 h post-injection, and more than 8% even at 48 h after injection for DACHPt/m [22]. This prolonged blood circulation of DACHPt/m was reasonably associated with the high kinetic stability of the micelles in phosphate buffered saline at 37 °C [22].

The accumulations of oxaliplatin and DACHPt/m in normal tissues (kidney, liver, spleen, and muscle) and solid tumor (C-26 cells) are shown in Fig. 2. Oxaliplatin was rapidly distributed to each organ in agreement with its rapid plasma clearance. In contrast, DACHPt/m showed cumulative accumulation in each organ and solid tumor ($p<0.001$) due to its remarkably prolonged blood circulation time, and the Pt level in the liver, spleen, and tumor continuously increased up to approximately 48 h after injection (Fig. 2). Consequently, the DACHPt/m exhibited 20-, 4-, and 25-fold higher accumulation in the liver, spleen, and tumor, respectively, than oxaliplatin at 48 h after injection. To assess the selectivity to the solid tumor, the
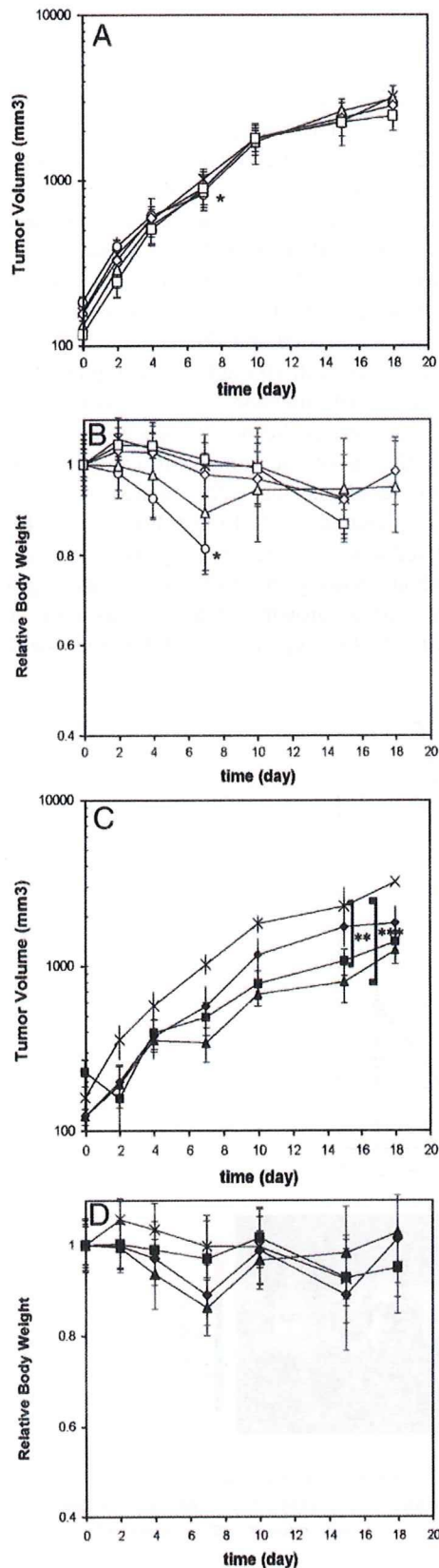

Fig. 5. Antitumor activity of DACHPt-loaded micelle (DACHPt/m) prepared with PEG-*b*-P(Glu) 12–20 against s.c. C-26 tumor model ($n=6$). Saline(×); oxaliplatin at 10 mg/kg(○): 6 mg/kg(△); 4 mg/kg(◇); 2 mg/kg(□). DACHPt-loaded micelle (DACHPt/m) 12–20 at 6 mg/kg(▲); 4 mg/kg(♦); 2 mg/kg(■). A. Tumor volume (mm³) for oxaliplatin treatment; B. Relative body weight of mice for oxaliplatin treatment; C. Tumor volume (mm³) for DACHPt/m treatment; D. Relative body weight of mice for DACHPt/m treatment. Data are expressed as averages±S.D. *Toxic death. **$p<0.01$. ***$p<0.005$.

accumulation ratios and area under the Pt concentration-time curve (AUC) ratios of the tumor to normal tissues at 48 h after injection are summarized in Table 2. The area under the Pt concentration-time curve was calculated based on the trapezoidal rule up to 48 h. As shown in Table 2, the tumor to kidney, liver and spleen ratios were lower than 1 for oxaliplatin, suggesting no selectivity to the tumor. In contrast, the DACHPt/m exhibited accumulation and AUC ratios higher than 1.0, suggesting its selective accumulation in the tumor.

3.2.2. Effect of P(Glu) block length on the biodistribution of micelles

The biodistribution of the micelles prepared from PEG-*b*-P (Glu) with different p(Glu) block units in tumor-bearing mice was examined and is shown in Fig. 3. The Pt accumulation levels were studied at 24 and 48 h. All the DACHPt/m formulations showed elevated Pt levels at the tumor (Fig. 3A and B). Importantly, the amount of Pt in liver was directly correlated with the length of the p(Glu) block forming DACHPt/m. The tumor targeting efficiency of the micelles was estimated by calculating the ratio of the accumulated dose in the tumor site against the accumulated dose in the organs (Fig. 3C and D). From these results, DACHPt delivery to the tumor site by a micellar carrier seems to be extremely efficient, since all the micelles showed higher tumor/organ accumulation ratios. This efficiency was maximized for the PEG-*b*-P(Glu) 12–20-micelle formulation showing the lowest non-specific accumulation in

normal tissues, thus achieving the highest relative tumor targeting. Such enhanced tumor targeting will permit expanding the therapeutic window of the micelle.

3.3. Antitumor activity

To evaluate the antitumor activity of DACHPt/m, CDF1 mice ($n=6$) bearing subcutaneous C-26 cells were treated i.v. four times at 2-day intervals with oxaliplatin at doses of 2, 4, 6, and 10 mg/kg or DACHPt/m (prepared with PEG-*b*-P(Glu) 12–40 and 12–20) at doses of 2, 4, and 6 mg/kg on a Pt basis. Each drug was intravenously injected on days 7, 9, 11, and 13 after inoculation, and the tumor volume after the treatment by oxaliplatin or DACHPt/m with PEG-*b*-P(Glu) 12–40 and 12–20 is shown in Figs. 4 and 5 (A and C), respectively. The relative body weight after the treatment was also monitored and shown in Figs. 4 and 5 (B and D).

The mice treated with 10 mg/kg of oxaliplatin showed toxic death after the fourth injection. Although animals treated with lower oxaliplatin doses did not show significant body weight loss, no inhibition of the tumor growth rate was observed ($p>0.05$). In contrast, the mice treated with 2 mg/kg of DACHPt/m prepared with PEG-*b*-P(Glu) 12–40 achieved significant reduction in the tumor growth rate ($p<0.001$ at day 14) without showing any body weight loss (Fig. 4C and D). Even higher tumor growth inhibition was observed for the mice treated with 4 mg/kg of PEG-*b*-P(Glu) 12–40 DACHPt/m
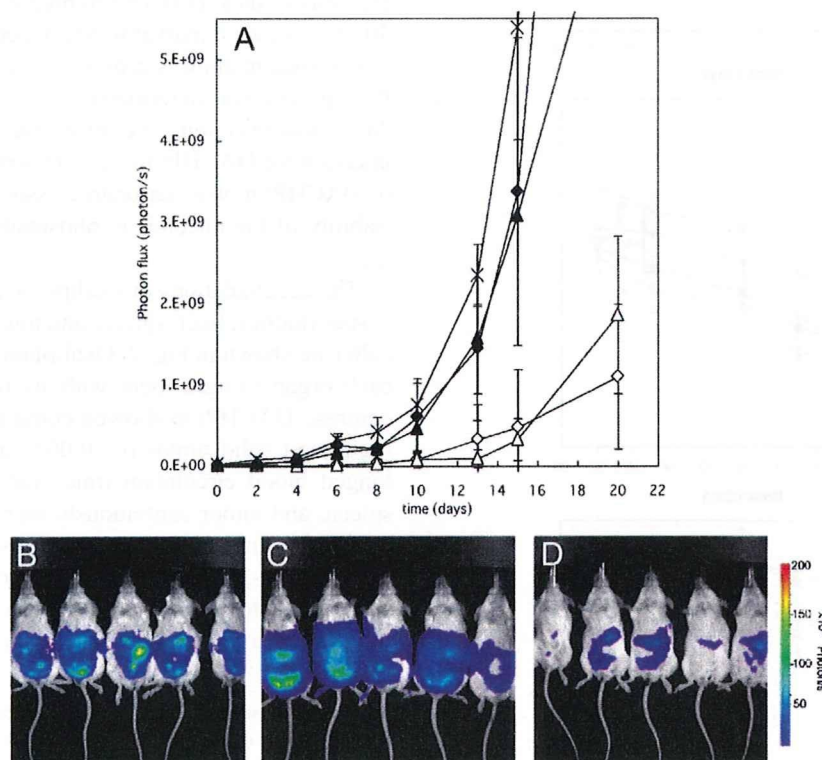

Fig. 6. Antitumor activity of DACHPt-loaded micelle (DACHPt/m) prepared with PEG-*b*-P(Glu) 12–20 against i.p. HeLa-Luc metastases ($n=5$). A. Relative photon flux from intraperitoneal metastatic sites of HeLa-luc *in vivo* treated with oxaliplatin or DACHPt-loaded micelle (DACHPt/m): Saline(×); oxaliplatin at 6 mg/kg(▲); 4 mg/kg(♦); DACHPt/m 12–20 at 6 mg/kg(△); 4 mg/kg(◇). Data are expressed as averages±S.D. *In vivo* bioluminescent images from HeLa-Luc i.p metastases at day 15: B. Saline; C. oxaliplatin 6 mg/kg; D. DACHPt/m 12–20 at 6 mg/kg.

($p<0.001$ at day 14); however, the 20% body weight loss after fourth injection suggests toxicity intensification. Increasing the DACHPt/m dose to 6 mg/kg resulted in 4 toxic deaths at day 8. The PEG-*b*-P(Glu) 12–20 micelle formulation reduced the toxicity while retaining the antitumor activity of the micelle (Fig. 5C and D). At 2 mg/kg or 4 mg/kg, this micelle formulation showed improved antitumor effect ($p<0.05$ at day 15 for 2 mg/kg; $p<0.01$ at day 15 for 4 mg/kg) compared with oxaliplatin without showing any body weight loss. At 6 mg/kg, the best tumor growth rate reduction was achieved ($p<0.005$ at day 15). The highest dose of this formulation in this experiment did not reach the lethal dose. Thus, PEG-*b*-P(Glu) 12–20 formulation for DACHPt/m seems to radically reduce drug toxicity with maintaining its potent antitumor effect, thus enlarging the therapeutic window. In addition, toxic death with DACHPt/m appeared at lower drug equivalent concentration than with oxaliplatin mainly due to the extremely high plasma AUC of DACHPt/m [22], but also because oxaliplatin is a prodrug of DACHPt. Thus, even though the drug equivalent of DACHPt/m to induce toxic death should be compared with DACHPt, it is very difficult to administer DACHPt alone due to its poor solubility.

Since DACHPt/m prepared with PEG-P(Glu) 12–70 showed higher accumulation to the liver and spleen than DACHPt/m prepared from PEG-P(Glu) 12–20 and 12–40, it will probably not increase the efficiency of the carrier. Therefore, its antitumor activity was not tested.

3.4. Antitumor activity in a bioluminescent intraperitoneal metastasis model

To evaluate the *in vivo* antitumor effect of DACHPt/m on multiple metastases generated from i.p inoculated Hela-Luc cells, SCID mice ($n=5$) were treated with free oxaliplatin or DACHPt/m beginning on day 4 post-injection. Mice with images indicating a successful i.p. inoculation on day 0 and showing *in vivo* evidence of metastasis by day 4 were placed in the drug treatment group. Free oxaliplatin or DACHPt/m were administered i.v a total of three times on day 0, 2, and 4. To quantify the bioluminescent data from metastasis, the photons emitted from the ROI in the whole animal (ventral images) were measured. The mean total photons/s were calculated from all mice. The *in vivo* bioluminescent data indicated that there was a 10-to 50-fold drop in the signal after DACHPt/m treatment (Fig. 6A). Images taken on day 15 (Fig. 6B, C, and D) indicated that DACHPt/m reduced tumor spreading in the peritoneal cavity, showing their strong growth inhibitory effect against the metastatic tumors.

4. Discussion

DACHPt/m were designed to have an extended blood circulation and a selective and high accumulation at the tumor site by the EPR effect. The average diameter of 40 nm and the hydrophilic PEG shell surrounding the micelle core are determinant features of DACHPt/m to avoid the uptake by the RES. Moreover, the sub-100 nm size of micellar nanocarriers might be optimal to achieve a remarkably high tumor extra-

vasation efficiency and deep tumor penetration regardless of the tumor type [26]. The pharmacokinetic parameters of polymeric micelles are significantly modulated by the copolymer architecture. In this regard, the length of the micelle core-forming block not only determines the drug loading capacity of the micelle but also contributes largely to the physicochemical properties of the micelles, whereas PEG length and PEG surface density of micelles have been strongly associated with their long-circulating properties [27,28]. In this study, we prepared DACHPt/m using PEG-*b*-P(Glu) bearing different lengths of p (Glu) chain. We found that this variation considerably influences the biodistribution of micelles and thereby their antitumor activity as well as the final therapeutic window.

Drug dosage in chemotherapy is decided in part based on the competing goals of maximizing the death of malignant cells while minimizing damage to healthy cells. In the case of oxaliplatin, the major and most frequent dose-limiting toxicity observed in clinical trials was neurotoxicity [1]. Toxicological studies performed on rats with cisplatin and oxaliplatin demonstrated that the main target of neurotoxicity was the dorsal root ganglion (DRG) [29]. Although cisplatin accumulated in the DRG at a higher extent than oxaliplatin, the latter displayed more morphometric changes to the DRG after an 8-week recovery period, and this was correlated with a greater retention of oxaliplatin by the DRG in comparison with cisplatin. In contrast, neurotoxic studies revealed that CDDP-loaded micelles did not show any neurotoxicity or neuronal degeneration in rats [21]. This result might be attributed to the marked restriction of platinum accumulation into nervous tissue for the CDDP-loaded micelle, owing to the micelle size and its hydrophilic surface. Since CDDP-loaded micelles and DACHPt/m showed comparable prolonged blood circulation, preferential tumor targeting, and low accumulation in organs (Fig. 2) [20], similar reduction in the platinum accumulation at nervous tissue should be expected for DACHPt/m. Moreover, it has also been suggested that the oxalate group on oxaliplatin might immobilize calcium ions, thereby altering the amplitude of voltage-gated sodium channels of neurons [30]. The absence of an oxalate group in the DACHPt/m formulations eliminates this kind of neuronal damage.

The use of oxaliplatin is also associated with the development of severe sinusoidal injury, an aspect that had not been considered in the earlier clinical trials of oxaliplatin [31,32]. In this regard, the CDDP-loaded micelle prepared with PEG-*b*-P(Glu) 12–40 has shown transient hepatic dysfunction in rats directly related to accumulation of the micelle in liver [21]. In the present study, DACHPt/m prepared with PEG-*b*-P(Glu) 12–40 showed biphasic behavior in liver accumulation, and the Pt level in the liver remarkably increased after 8 h post-injection (Fig. 2B). Thus, the avoidance of liver uptake would be critical for the development of a clinically effective DACHPt/m formulation. We previously reported that the CDDP-loaded micelles also showed rapid accumulation of the micelle in the liver due to the morphological changes of the micelle accompanied by the release of CDDP during circulation [20]. However, such liver accumulation of the CDDP-loaded micelles was reduced for the micelle formulation from PEG-*b*-P(Glu) with a longer PEG segment [20]. Thus, the

coverage of the nanoparticles with PEG palisades is likely to be a crucial factor in the reduced liver accumulation. In this study, we evaluated the effects of the P(Glu) lengths of PEG-*b*-P(Glu) on the accumulation of the micelles in normal tissues and tumors. As a result, the micelles prepared with PEG-*b*-P(Glu) 12–20 showed considerably reduced accumulation in the liver (Fig. 3), resulting in critically reduced toxicity and, in particular, permitted a dosage increase (Fig. 5). Possibly, the use of PEG-*b*-P(Glu) with shorter P (Glu) segments may allow the formation of DACHPt/m with effective surface coverage by PEG probably due to reduced micellar core size, leading to reduction of the liver accumulation of the micelles.

DACHPt/m, prepared with PEG-b-P(Glu) 12–40 or 12–20, presented a remarkable, statistically relevant *in vivo* antitumor activity (Figs. 4 and 5), whereas free oxaliplatin failed to suppress tumor growth. The improved performance of DACHPt/m could be attributed to several aspects. The most distinguishable one is the high and preferential accumulation of DACHPt/m in the tumor due to the prolonged circulation of micelles in the bloodstream as well as the aforementioned EPR effect. In this study, DACHPt/m showed 10 times higher tumor accumulation than free oxaliplatin after 24-h post-injection, and such accumulation was maintained for an extended period (Figs. 2 and 3). On the other hand, free oxaliplatin was rapidly cleared from the bloodstream and the drug level at the tumor site was particularly low (Fig. 2). This accumulation level may be lower than the minimal amount needed to attain an efficient *in vivo* antitumor activity.

The avoidance of permanent drug inactivation by protein binding through the complexation of the platinum to the carboxylic groups in the micelle core could also be responsible for the improved biological performance of DACHPt/m over oxaliplatin. It was previously reported that, immediately after a 1 h infusion of oxaliplatin, approximately 5–30% of the drug is unbound, 10–30% is protein-bound, and 40% form complexes with hemoglobin and small molecular weight compounds in erythrocytes. Three hours later, no oxaliplatin is detectable in the plasma ultrafiltrate and only 10% is detectable in urine [33,34]. Furthermore, as many as 17 biotransformation products of oxaliplatin have been described (conjugation with methionine, cysteine, glutathione, and other low molecular weight species), but only the minor complexes $DACHPtCl_2$, $[DACHPt(H_2O)Cl]^+$ and $[DACHPt(H_2O)_2]^{2+}$ retain the ability to bind to DNA to exert the cytotoxic activity [35,36]. Among them, the dihydroxy product of oxaliplatin has been shown to have significantly greater cellular uptake and cytotoxic properties than its parent compound [37]. However, it represents a very small amount of the total plasma platinum pool after oxaliplatin administration, and therefore might not be a determinant for oxaliplatin cytotoxicity. Moreover, the formation process of $[DACHPt(H_2O)_2]^{2+}$ involves the formation of a reversible intermediate, oxalato monodentate compound, and the dissociation constant for the ring-opening step is below physiological pH ($p\dot{K}a = 7.16$). This implies that at physiological pH, the reaction favors the deprotonation of the open-ring form and the subsequent formation of the dihydroxy complex, whereas under the acidic conditions of solid tumors, ring-closure is favored and the rapid formation of oxaliplatin

would be expected [38]. For DACHPt/m, the biotransformation products might be considerably different from those of oxaliplatin, and probably affect the *in vivo* performance of the drug. Since the discharge of DACHPt products from the micelle core occurs only after cleavage of the polymer-metal complex by chloride ions, and this release is enhanced at low pH, DACHPt/m probably set up conditions that favor the formation of active complexes of oxaliplatin, including the highly active [DACHPt $(H_2O)_2]^{2+}$, leading to an improved efficacy of the drug. Moreover, selective intracellular release of DACHPt complexes might occur after internalization of the micelles by endocytosis in cancer cells. As a result, DACHPt complexes may avoid extracellular inactivation and may readily induced intracellular damage.

Since systemic chemotherapy is not regarded as curative in patients with metastatic tumors and all the established therapies show low efficiency at the late stage of the disease, the antitumor activity of DACHPt/m against an i.p. metastatic tumor model was evaluated to test the potential use of micelles as a therapeutic strategy. Monitoring the development of metastatic disease is currently possible *in vivo* with the use of small animal imaging technologies including bioluminescent imaging. The results demonstrate that free oxaliplatin failed to suppress HeLa-Luc metastatic growth at any dose, whereas DACHPt/m showed a high antitumor activity while controlling tumor dissemination in the peritoneal cavity. This marked difference could be correlated to the extended blood circulation and preferential tumor accumulation of DACHPt/m, although further experiments are necessary to determine the effect of the metastatic disposition on the efficiency of the micelle. The present results revealed that DACHPt/m has a high level of antitumor activity not only on primary solid tumors but also against metastatic tumors, suggesting that DACHPt/m could be an outstanding drug delivery system for metastasis treatment.

In conclusion, we have demonstrated that decreasing the length of the core-forming block of DACHPt/m augmented their tumor specificity and drastically diminished their toxicity. Moreover, the high and preferential accumulation of the micelles at the tumor site resulted in considerable antitumor activity of DACHPt/m against primary and metastatic tumor models. Thus, DACHPt/m might be an exceptional drug delivery system for oxaliplatin active complexes.

Acknowledgments

References

[1] A. Ibrahim, S. Hirschfeld, M.H. Cohen, D.J. Griebel, G.A. Williams, R. Pazdur, FDA drug approval summaries: oxaliplatin, Oncologist 9 (2004) 8–12.
[2] J.M. Extra, M. Espie, F. Calvo, Phase I study of oxaliplatin in patients with advanced cancer, Cancer Chemother. Pharmacol. 25 (1990) 299–303.